

On the turbulent flow field over riblets of various groove sizes at low Reynolds number

J. H. Ng,^{*} R. K. Jaiman,[†] and T. T. Lim[‡]

Department of Mechanical Engineering, National University of Singapore

Abstract

In this work, low Reynolds number turbulent flow through a corrugated channel, formed by standard V-groove riblets, are investigated via direct numerical simulations (DNS). The simulations attempt to assess the variation of flow dynamics caused by a change in the characteristic size of the V-groove riblets. Such characterization of size effects provides a means to identify the local flow features arising from fluid-riblet interaction, and to investigate their relevance to the change in viscous drag and turbulence statistics. The present simulations confirmed an improved variation trend when the flow dynamics is examined in the light of the groove size. This suggests that the transition across the range of local flow regimes perceived by the V-groove riblets may be better characterized by the groove size, as compared to the spacing or height. At the lower end of the range of groove size considered, the profiles of turbulence statistics more or less resemble the plane channel flow, except for a systematic shift with the groove size. When the groove size becomes increasingly large, the lodging of near-wall flow structures and the generation of mean secondary flows tend to be more apparent. The collective impact of the lodging of flow structures and the mean secondary flow correlates with the increase in viscous drag, and leads to significant alterations of the turbulence statistics. In addition, the invigorated near-wall fluid motions due to their closer proximity with the groove surface can cause the formation of humps on the velocity fluctuation profiles. Lastly, two correlations as a function of the groove size are explored to illustrate their potential to capture the overall effects of riblets. Such correlations involving riblets of various sizes may provide insights on modeling fluid-riblet interaction in low Reynolds number turbulent channel flows.

^{*} ngjeehann@u.nus.edu

[†] Corresponding author: mperk@nus.edu.sg

[‡] mpelimtt@nus.edu.sg

I. INTRODUCTION

The ability to control the multitude of fluid flow phenomena has been a perpetual quest that mankind has delved into since the dawn of fluid study. In particular, flow over patterned surface is a fundamental problem that continues to be an active field of research owing to profound practical implications. Riblets, which are longitudinal striations of different cross-sections, have been a potential candidate for applications ranging from aircraft drag reduction at high Reynolds number [1, 2], to the mitigation of blood cell damage caused by flow-induced stress at moderate Reynolds number [3]. Grasping the flow field evolution with the characteristic size of riblets is pivotal to achieve the desired flow attributes in all these applications. Of particular interest in this work is to gain a more systematic understanding of fluid-riblet interaction in low Reynolds number turbulent flows, which may provide useful insights for improving the blood compatibility of cardiovascular devices via surface modification [4]. Interested readers may recap about the research progress from a few comprehensive reviews [5–10].

The immense amount of research in the past few decades has established that the drag reduction performance of riblets has a dependency on their size measured in wall units [11, 12], i.e. normalized by the viscous length scale ν/u_τ where ν is the kinematic viscosity and $u_\tau = \sqrt{\tau_w/\rho}$ is the friction velocity derived from the wall shear stress τ_w and fluid density ρ . Typically, the spacing s or the height h of riblets measured in wall units is taken as the reference length scale to denote the size. As the size gets progressively larger, the flow field over riblets can exhibit different physics ranging from one dominated by viscous effects (*viscous regime*) to another strongly influenced by non-linear inertial effects (*k-roughness regime*). Such nature gives rise to the diverse viscous drag behavior of riblets with their size [13], and in turn it renders the study and understanding of the physics of flow around riblets an arduous endeavor. Apart from the size, the shape of the riblets can lead to a varying degrees of performance [14, 15]. To date, the thin blade geometry at the optimum size produces up to 9.9% reduction of turbulent skin friction drag [16].

In most of the earlier works, the focus has been on relating the change in drag with either s^+ or h^+ to determine the optimum riblet geometry for drag reduction, while only a handful of studies are devoted to elucidate the drag reduction mechanisms. The *protrusion height* concept [17–19] states that riblets produce viscous drag reduction owing to their higher

cross-flow resistance. Unfortunately, this concept rests on the premise that the riblets are small enough to not be affected by inertial effects. As the size gets larger, the possibility that additional mechanisms or flow features that arise from inertial effects come into play cannot be discounted. Choi *et al.* [20] postulated that near-wall streamwise vortices tend to lodge in the groove when the riblet spacing s becomes larger than their average diameter of 30 wall units. On the other hand, Goldstein and Tuan [21] reported that widely spaced riblets generates secondary flow due to the less effective damping of cross-flow fluctuations. Although the nature of influence of these proposed mechanisms on the viscous drag are mainly said to be contingent on s^+ , their variation trend with the characteristic size of riblets is still unclear.

Although the conventional description of the riblet size in terms of s^+ and h^+ may be immaterial when considering the scaling of drag reduction curves, the choice becomes imperative if the aim is to elucidate the flow dynamics across a range of riblet geometries. The rationale is that the fluid-riblet interaction of various geometries could exhibit a diverse nature. In this connection, there is a need to assign a suitable dimensionless length scale, which also acts as the effective *local* Reynolds number, to delineate the overall effects of riblets. García-Mayoral and Jiménez [22] have recently proposed an alternative length scale l_g^+ , defined as the square-root of the riblet groove cross-sectional area A_g measured in wall units (see the schematic diagram alongside Fig. 1), to characterize the riblet size. The improved scaling of drag reduction curves from past experiments enabled them to pinpoint the onset of breakdown of the *viscous regime* at $l_g^+ \approx 11$. Unfortunately, their simulations are limited to thin blade riblets with a height-to-spacing ratio h/s of 0.5, i.e. l_g/s is constant. Hence, it is rather difficult to confirm whether scaling with l_g^+ offers any benefit over s^+ or h^+ , in terms of characterizing the flow dynamics imposed by V-groove riblets.

The first objective of the present work is to investigate the evolution of the flow dynamics at low Reynolds number when the characteristic size of V-groove riblets is changed systematically. Once the variation trend is established, the next objective is to explore the relevance of the various flow features stemming from fluid-riblet interaction on the viscous drag and turbulence statistics. The objectives are achieved by performing direct numerical simulations (DNS) of fully-developed turbulent channel flow over six V-groove (triangular) riblet configurations. These configurations have groove sizes denoted by l_g^+ that span both drag-reducing and drag-increasing regimes when simulated at a bulk Reynolds number Re_m

of either 1842 or 2800. Of particular note is that the riblet configurations comprise of two different h/s ratios to ascertain the effectiveness of l_g^+ in capturing the influence of both s and h . It is worthwhile to mention that the characterization of the flow dynamics imposed by riblets, or any other patterned surface, is essential to achieve the desired flow attributes in various applications of interest. It can also provide some prospects for the development of turbulence models to ease the computational intensity of simulations of high Reynolds number flows over riblets.

II. METHODOLOGY

The present study considers a fully-developed channel flow of an incompressible fluid. In the Cartesian coordinate system, x , y and z denote the streamwise, wall-normal and spanwise directions, respectively. The origin of the coordinate axes is located at the center of the inlet plane as depicted in Fig. 1. All the flow quantities, henceforth, are normalized by outer scales represented by the channel half-width δ and the bulk streamwise velocity U_m . Accordingly, the flow Reynolds number is defined as $Re_m = U_m \delta / \nu$, where ν is the kinematic viscosity. The governing equations can be written in non-dimensional form as:

$$\nabla \cdot \mathbf{V} = 0 \quad (1)$$

$$\frac{\partial \mathbf{V}}{\partial \mathcal{T}} + \mathbf{V} \cdot \nabla \mathbf{V} = -\nabla p + \frac{1}{Re_m} \nabla^2 \mathbf{V} + \mathcal{F} \mathbf{e}_x \quad (2)$$

where $\mathbf{V} = (u, v, w)$, p and \mathcal{T} are the non-dimensional velocity vector, pressure and time, respectively. u , v , and w are the respective components of \mathbf{V} in the streamwise (x), wall-normal (y), and spanwise (z) directions. $\mathcal{F} > 0$ is a prescribed external force to drive the flow through the channel, and \mathbf{e}_x is the unit vector in the x direction.

Periodic boundary conditions are imposed in the x and z directions, while a no-slip condition is enforced on the two walls. In the present work, the forcing term \mathcal{F} is adjusted dynamically to maintain a constant flow rate (CFR) through the channel. It is evaluated based on the deviation of bulk velocity U_m at each time step. Accordingly, \mathcal{F} can be perceived as a time-dependent pressure gradient that balances the wall shear stress τ_w in a time-averaged sense. The CFR forcing strategy is chosen to allow a direct change of wall shear stress during the course of the simulation. Although not shown here, the temporal fluctuations of U_m in all cases are fairly small (standard deviation is $< 0.02\%$ of the mean),

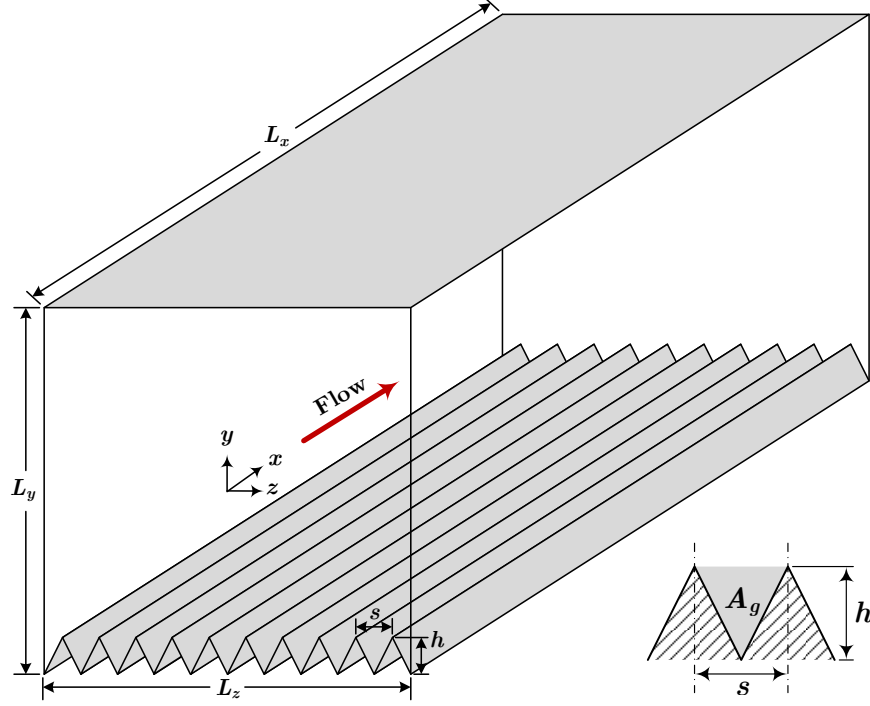


FIG. 1. Computational domain of the turbulent channel flow with V-groove riblets mounted on the bottom wall.

while the time-averaged values of \mathcal{F} and τ_w differ by less than 0.5%. The V-groove riblets are mounted on the bottom wall to allow a direct comparison of flow properties over two different surface geometries under the same level of uncertainty. Note that the channel height $L_y = 2\delta$ is measured from the valley of the riblets to the top wall as illustrated in Fig. 1. The percentage drag reduction is then computed from the difference between the time-averaged drag on the two walls. The drag is derived from the stress tensor $\sigma = \nu(\partial u_i/\partial x_j + \partial u_j/\partial x_i)$, in which the pressure drag is non-existent because of the streamwise homogeneity of riblets.

Since riblets are created only on one of the walls, the flow is asymmetric about the channel centerline which results in different friction velocities on the two walls. In actual fact, the friction velocity on the smooth wall tends to increase with the size of riblets. Such physical effect may be explained in part by a reduction in the *hydraulic diameter* d_h of the channel [23]. In a way, this idea can account for the higher viscous drag produced by riblets in laminar channel flows, and it is in accord with the notion of an increase in the wetted surface area [24, 25]. Accordingly, it may be reasonable to say that part of the change in viscous drag produced by riblets in internal flows can be attributed to the modification of

the *hydraulic diameter*. In this respect, the percentage drag reduction computed against the baseline channel flow would contain an anomaly because of the inherently different d_h . On the contrary, computation within a single domain offers the advantage of alleviating such problem, because the same effect is exerted on both walls.

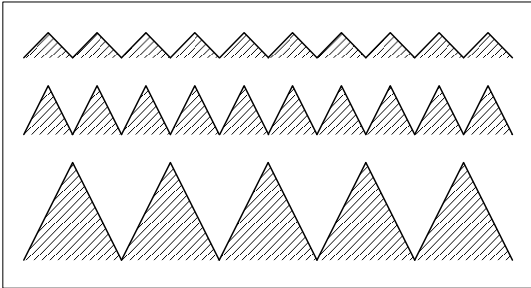
The size of the V-groove riblets is defined using the dimensionless length scale l_g^+ proposed by García-Mayoral and Jiménez [22]. This length scale is expressed as the square root of the groove cross-sectional area A_g (see the schematic diagram alongside Fig. 1) measured in wall units, i.e. $l_g^+ = \sqrt{A_g} u_\tau / \nu$. Their rationale of using A_g as an indicator of the riblet size is to collectively capture the influence of riblet spacing s and height h . Note that the definition of l_g^+ in wall units is computed with respect to the surface-averaged friction velocity on the riblet wall in this work. Unless otherwise stated, flow quantities stated with an overbar, i.e. $\overline{(\cdot)}$, denote the *mean* or *time-averaged* value, whereas those written with a prime, i.e. $(\cdot)'$ refer to the *fluctuating* part. Root-mean-square (rms) quantities are affixed with a subscript, i.e. $(\cdot)_{rms}$. Flow quantities measured in *wall units* or normalized by the inner scales derived from ν and u_τ are indicated with a + superscript, i.e. $(\cdot)^+$, throughout this paper.

A. Numerical method and solver

The solver *nek5000* [26] employed in this work is based on the spectral element spatial discretization scheme [27], but uses the Gauss-Lobatto-Legendre (GLL) quadrature points within each local, non-overlapping element generated by decomposing the global domain [28]. The spectral element method combines the accuracy of spectral methods and the generality of the finite element method. As a result, it can treat a wide class of geometrically and physically complex problems while maintaining spectral-like accuracy and rate of convergence [29]. Furthermore, it is advantageous for solving unsteady incompressible flow problem at moderate Reynolds number due to its non-dissipative and non-dispersive properties [30]. In the present work, a $\mathbb{P}_N - \mathbb{P}_N$ formulation is implemented where the velocity and pressure field are represented by a Lagrange polynomial of degree N . The time integration is performed via a high-order operator-integration-factor splitting (OIFS) method [31] with an implicit linear Stokes solver, coupled with an explicit sub-integration of the non-linear advective term [32]. Specific formulation and implementation details of the solver can be found in [32–34].

TABLE I. The six V-groove riblet configurations considered in the current parametric study. Figure on the right shows the schematic view of the three physical configurations of V-groove riblets under the same scale.

Case	Re_m	s	h
I	1842	0.2δ	0.1δ
II		0.2δ	0.2δ
III		0.4δ	0.4δ
IV	2800	0.2δ	0.1δ
V		0.2δ	0.2δ
VI		0.4δ	0.4δ



B. Numerical setup and configurations

In the current parametric study, V-groove riblets with three different combinations of physical spacing s and height h have been simulated at two bulk Reynolds numbers $Re_m = 1842$ and 2800 . Table I describes the physical dimensions of the six configurations denominated as Cases I to VI. A schematic diagram illustrating the relative appearances of the riblets is provided on the side of the table. One of the configurations denoted as Case II follows closely the reference DNS of Chu and Karniadakis [25]. This flow configuration is chosen as a guideline to assess the current simulation setup using the spectral element solver. In Case II, the riblet height and spacing are both 0.2δ . There are 10 riblets across the span as depicted in Fig. 1. Also, the riblets are introduced into the fluid domain explicitly without any form of modeling. Although explicitly resolving the riblet profile inevitably slows down the convergence of solutions, the improved accuracy of the near-wall flow field is undoubtedly crucial to elucidate the nature of turbulence in the presence of riblets.

Two separate simulations denoted as Cases I and III are also performed to contrast the flow fields at the same bulk Reynolds number $Re_m = 1842$ or $Re_\tau \approx 122$. These simulations facilitate the identification of the flow features responsible for the vast change in flow behavior. The remaining three configurations, i.e. Cases IV to VI, are simulated at $Re_m = 2800$ or $Re_\tau \approx 180$ to obtain a more representative turbulent flow field, and to include the effects of Reynolds number. Although the current work is limited to moderate Reynolds

number, earlier studies have noted that such computations could be adequate for studying flow structures [35]. García-Mayoral and Jiménez [36] have demonstrated that the physical descriptions deduced at $Re_\tau \approx 180$ are essentially correct. Noticeable discrepancies would probably manifest when the Reynolds number is far higher, i.e. $Re_\tau > 10^3$ [37, 38].

As in the reference DNS [25], the computational domain has dimensions of $L_x = 5\delta$, $L_y = 2\delta$ and $L_z = 2\delta$ in the x , y and z directions, respectively. This translates to $L_x^+ \approx 650$ and $L_y^+ = L_z^+ \approx 260$ with respect to the smooth top wall. The current domain extent in the homogeneous directions is about two and a half times larger than the *minimal flow unit* ($L_x^+ \approx 250 \sim 350$ and $L_z^+ \approx 100$) found by Jiménez and Moin [39]. Since a higher mesh resolution is essential to resolve the flow field around riblets, the small domain allows the simulations to complete within a reasonable time. The articulation by Gatti and Quadrio [40] on the greater computational efforts expended on simulating the initial transient in a larger domain applies to the present work as well. Having said that, an assessment on the impact of domain size on the relevant flow properties is presented in Appendix II C. The other five configurations are also simulated with the same domain size of $5\delta \times 2\delta \times 2\delta$ to maintain consistency.

For the simulations at $Re_m = 1842$, the domain is partitioned into $21 \times 14 \times 20$ elements in the x , y and z directions, respectively. The total number of grid points in each orthogonal direction x , y and z is 190, 127 and 181, respectively after including the GLL nodes within each element generated based on a 9th order Lagrangian polynomial. On the other hand, two additional layer of elements are added in the wall-normal direction for the simulations at $Re_m = 2800$, increasing the number of grid points to 145. In Case II, the average resolution in the streamwise and spanwise directions are respectively $\Delta x^+ \approx 3.4$ and $\Delta z^+ \approx 1.4$ with reference to the friction velocity on the smooth wall. The resolutions become $\Delta x^+ \approx 2.3$ and $\Delta z^+ \approx 1.0$ when computed using the surface-averaged friction velocity on the riblet wall. In the wall-normal direction, a hyperbolic sine function is used to distribute the element size such that more grid points are clustered near the two walls. Accordingly, the first element adjacent to the riblet wall which comprises of 10 grid points is below $y^+ = 5$, and the first grid point away from the riblet wall is at $y^+ \approx 0.12$. On the other hand, the average wall-normal resolution near the channel centerline is $\Delta y^+ \approx 5$.

The mesh resolutions in all configurations, especially near the riblets, are made sufficiently high to avoid under-resolved simulation that can give rise to undesirable wiggles and over-

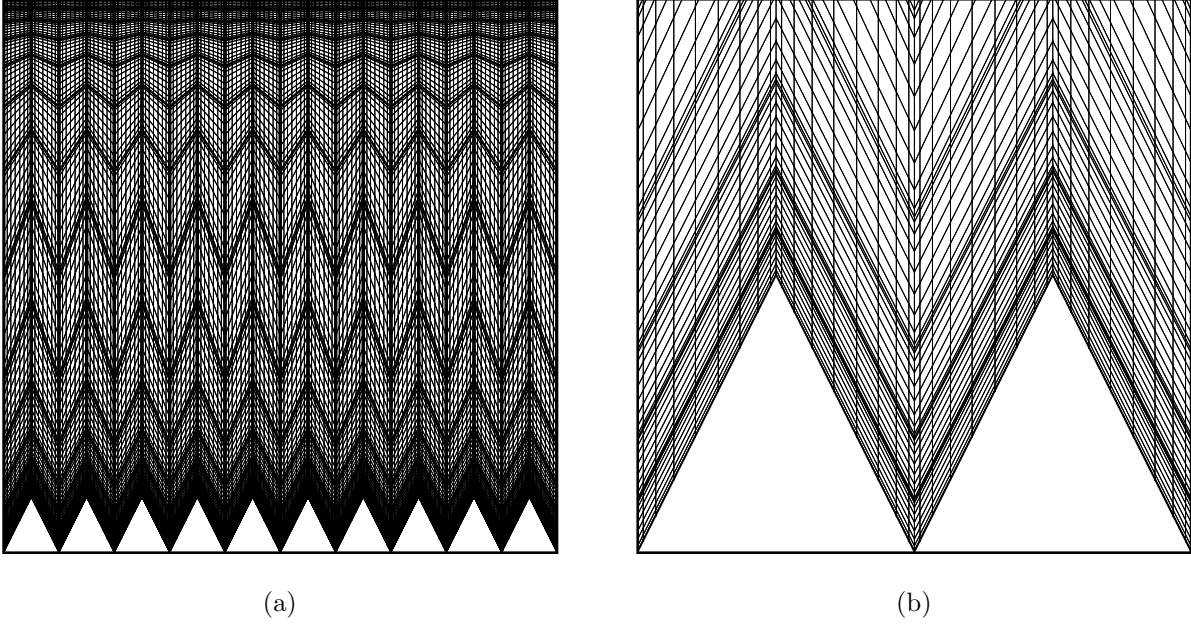


FIG. 2. (a) Spectral element mesh for the simulation of Case II ($s = 0.2\delta$, $h = 0.2\delta$), and (b) Close-up view of the mesh near the V-groove riblets.

or under-predicted profile of streamwise velocity fluctuations u' , see section 9.3.1 in the book written by Karniadakis and Sherwin [41]. In particular, the mesh resolution is designed to be higher than the plane turbulent channel flow to accommodate the possible reduction in scales when riblets are introduced into the flow domain. This coupled with the use of a 9th order spectral element discretization helps to enhance the accuracy of the simulations and to diminish dispersion errors [32]. Figure 2(a) depicts the generated spectral element mesh for Case II, while Fig. 2(b) shows a magnified view of the same mesh in the proximity of the riblets. Table II presents the computational mesh setups of the six riblet configurations.

The simulations of all six configurations are carried out for a non-dimensional period $TU_m/\delta = 750$ using the baseline turbulent channel flow solution at $Re_\tau \approx 180$ as the initial condition. The non-dimensional time step size $\Delta t U_m/\delta$ is 0.005 in all six configurations. At $Re_m = 2800$, this time step in wall unit, i.e. $\Delta t u_\tau^2/\nu \approx 0.06$, is much smaller than the value recommended by Choi *et al.* [20] ($\Delta t^+ \approx 0.4$) to accurately predict turbulence statistics of a plane channel flow. As the solver employs a characteristics-based time stepping method, i.e. the OIFS procedure, a less restrictive Courant or CFL number up to 4 is allowable [31, 42]. In the present set of simulations, the CFL number varies from 1 to 3 while the temporal discretization scheme attains a third-order accuracy. The average computation time of the

TABLE II. Computational mesh setups of the V-groove riblet configurations. The values in wall units are computed based on the surface-averaged friction velocity at the riblet wall.

Case	N_x	N_y	N_z	Δx_{min}^+	Δx_{max}^+	Δy_{min}^+	Δy_{max}^+	Δz_{min}^+	Δz_{max}^+
I				0.98	4.02	0.15	6.44	0.41	1.69
II	190	127	181	0.82	3.38	0.12	5.25	0.35	1.42
III				1.03	4.23	0.13	5.97	0.43	1.78
IV				1.46	6.01	0.19	8.64	0.61	2.53
V	190	145	181	1.29	5.29	0.16	7.26	0.54	2.22
VI				1.56	6.42	0.17	7.91	0.66	2.70

six configurations is about 10 seconds per time step when executed over 48 parallel processes.

C. Impact of domain size

In simulations of fully-developed turbulent channel flows with periodic boundary conditions, the domain size plays a pivotal role in determining the extent of boundary layer that possess “healthy” turbulence [43, 44]. Hence, a preliminary study is carried out to assess the impact of domain truncation on flow statistics. It begins with the baseline turbulent channel flow, followed by one of the V-groove riblet configurations. The assessment concerning the baseline configuration is achieved by comparing the simulations with domain sizes of $5\delta \times 2\delta \times 2\delta$ and $4\pi\delta \times 2\delta \times 2\pi\delta$ with similar mesh resolutions at $Re_m = 1842$ and 2800.

Figure 3 demonstrates that the effect of a smaller domain is noticeable mainly on the statistics of the streamwise velocity fluctuations u' , especially at $Re_m = 1842$ because of the smaller domain size in wall units, i.e. $L_x^+ \approx 650$ and $L_z^+ \approx 260$. The higher peak of u' is in line with the observation that the two-point correlation of u' (not shown here) does not decay to zero at one-half of the streamwise domain extent. On the other hand, the smaller domain size does not result in considerable disparity at $Re_m = 180$, because it is relatively large when translated to wall units, i.e. $L_x^+ \approx 930$ and $L_z^+ \approx 370$.

In a statistically stationary and fully-developed turbulent channel flow, the total shear stress comprises of the combined contribution by the mean viscous stress and the Reynolds stress is linear along the wall-normal direction. In Fig. 4, there is no noticeable discrepancy

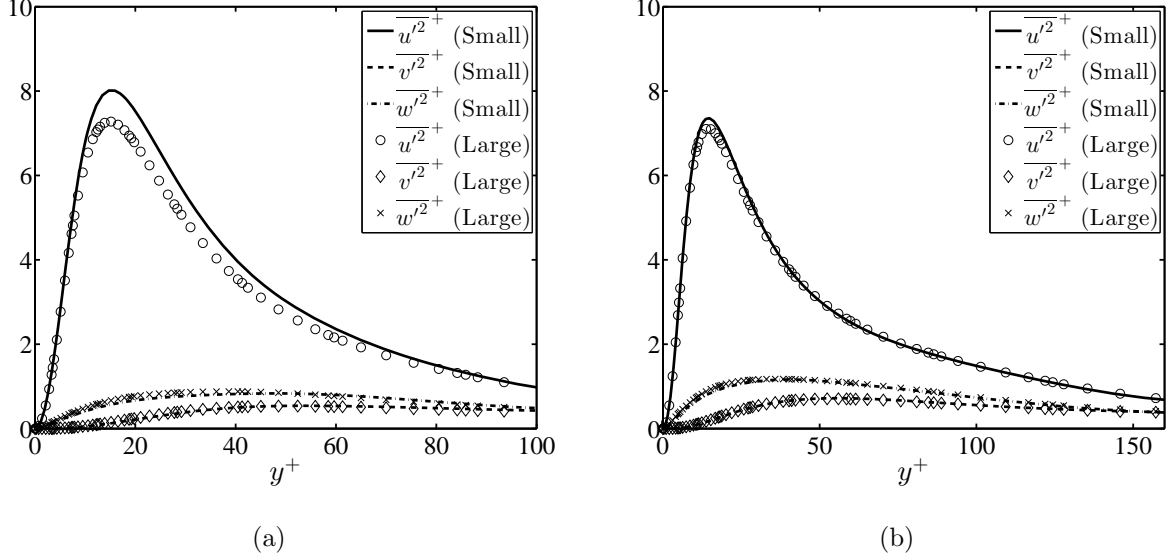


FIG. 3. Comparison of the mean-square velocity fluctuations profiles plotted in wall units acquired from simulations of the baseline turbulent channel flow with different domain sizes at: (a) $Re_m = 1842$, and (b) $Re_m = 2800$.

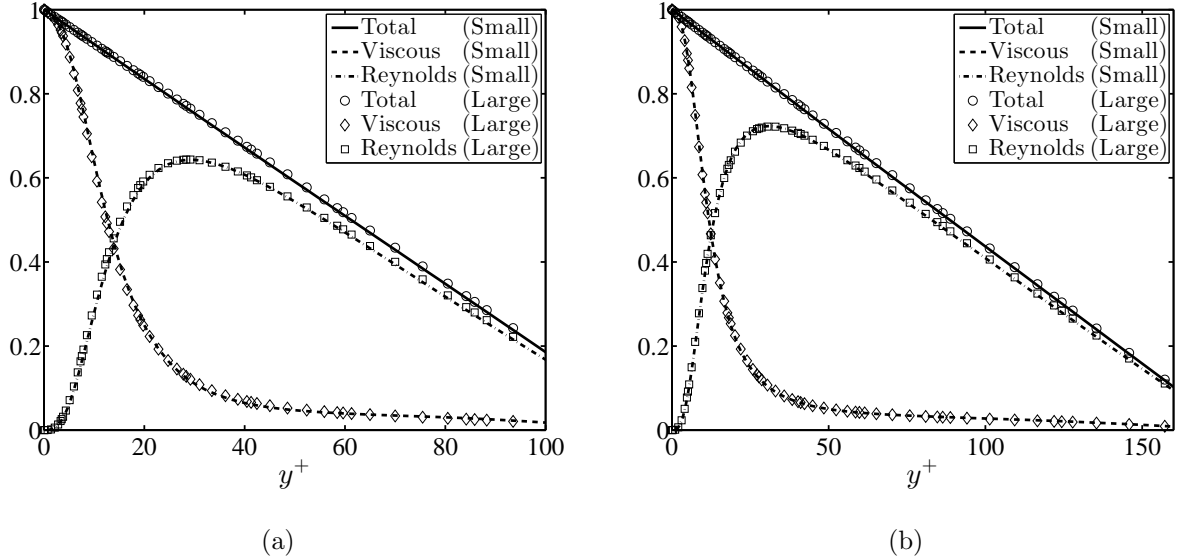


FIG. 4. Comparison of the time-averaged shear stress profiles plotted in wall units acquired from simulations of the baseline turbulent channel flow with different domain sizes at: (a) $Re_m = 1842$, and (b) $Re_m = 2800$.

between the two sets of shear stress profiles. The close agreement corroborates the finding by Gatti and Quadrio [40] that the variation in the skin friction coefficient C_f at $Re_\tau \approx 200$ is more or less unaffected by the domain size when $6 < L_x L_z / \delta^2 < 60$, see figure 3 in their

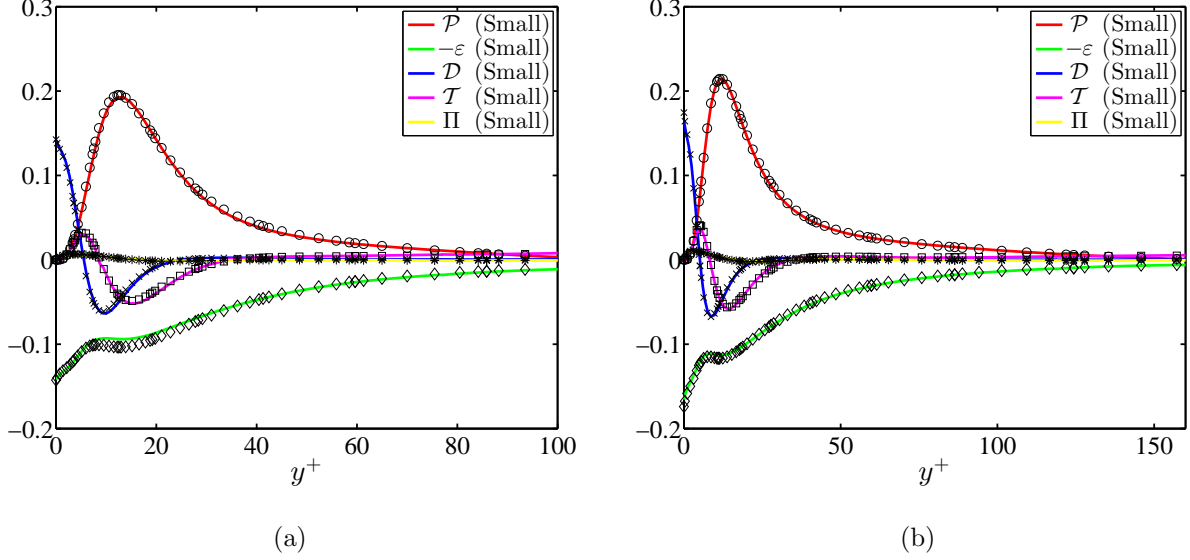


FIG. 5. Comparison of the budget of turbulence kinetic energy plotted in wall units acquired from simulations of the baseline turbulent channel flow with different domain sizes at: (a) $Re_m = 1842$, and (b) $Re_m = 2800$. The markers ($\circ, \diamond, \times, \square, *$) represent the corresponding profiles acquired from the larger domain configuration.

paper. In fact, they demonstrated that the uncertainty is almost canceled out when the drag reduction is computed under the same simulation condition. Another important metric to assess the implication of domain size is the budget of turbulence kinetic energy k which describes the energy transfer process instituted by the turbulent motions. The transport equation of k , encompassing the five terms \mathcal{P}_k , \mathcal{D}_k , \mathcal{T}_k , Π_k , and ε_k , is equivalent to equation (1) given by Mansour *et al.* [45]. Once again, Fig. 5 illustrates that the reduced domain size does not affect the turbulence processes considerably.

Apart from the baseline configuration, the riblet configuration denoted as Case II is also compared with another simulation performed in a domain that is one and a half times longer in the streamwise (x) and spanwise (z) directions. Figure 6 reveals no significant discrepancy between the two sets of simulation, probably because the stabilizing effect of riblets compensates, to some extent, the higher intermittency in the flow evolution. Judging from these assessments, the findings derived from the present simulations are expected to be marginally affected by the domain size. Although there might be more noticeable discrepancy if compare with an even larger domain simulation, the issue is not pursued further because it would deviate from the scope of the present work, apart from being too costly.

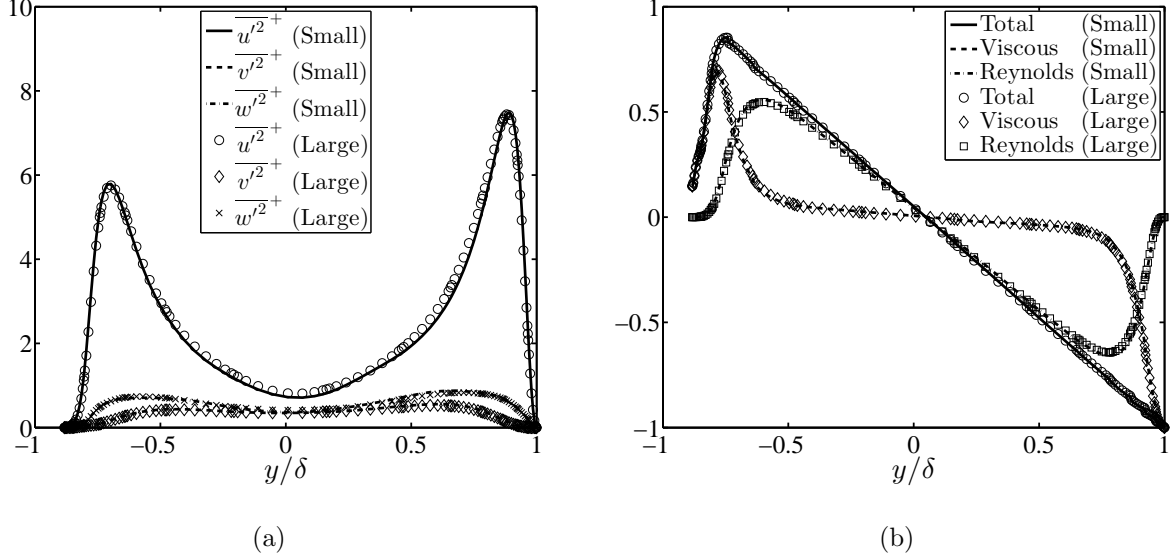


FIG. 6. Impact of domain size on the statistics of Case II ($l_g^+ \approx 12$) across the channel: (a) Mean-square velocity fluctuations, and (b) Time-averaged shear stresses. Note that the flow quantities are scaled in wall units using the friction velocity of the top (smooth) wall.

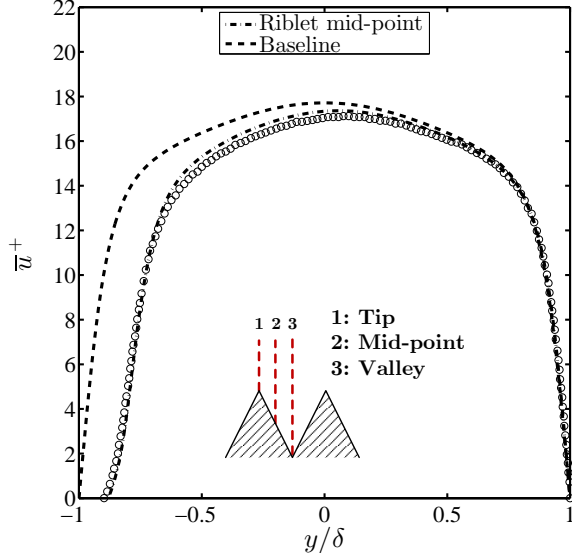
III. RESULTS AND DISCUSSIONS

The time averaging of flow quantities is performed within a non-dimensional time period TU_m/δ of 450 which corresponds to about 100 eddy-turnover time units. Furthermore, these statistical profiles have been spatial-averaged in the streamwise direction, and also “piecewise-averaged” in the spanwise direction that collapses the domain into one-half of a V-groove riblet. In the following discussions, the statistics are plotted at three spanwise positions, namely “tip”, “mid-point” and “valley” as illustrated schematically in Fig. 7(a).

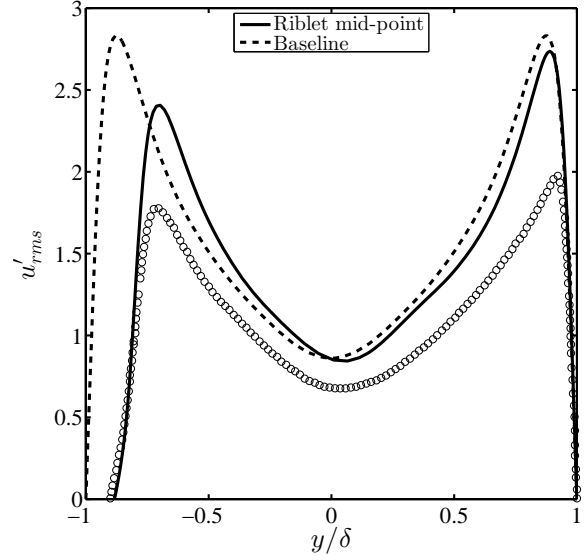
A. Benchmarking study

Case II in this parametric study represents a benchmarking configuration adapted from the work of Chu and Karniadakis [25], since their numerical framework was formulated in part using the spectral element method. The resulting riblet spacing and height in wall units are respectively $s^+ = 17.2$ and $h^+ = 17.2$, based on the surface-averaged friction velocity of the riblet wall. It is worthwhile to mention that the reference profiles reproduced in the present paper could contain a small degree of error arising from the digitization process.

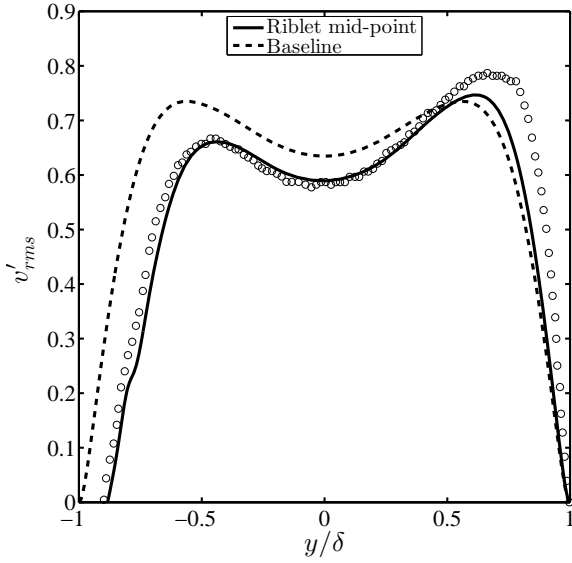
Figure 7 depicts the profiles of mean streamwise velocity, root-mean-square velocity fluc-



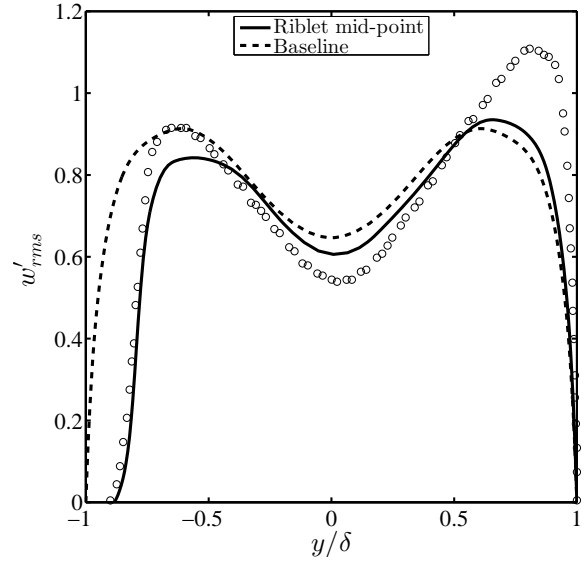
(a)



(b)



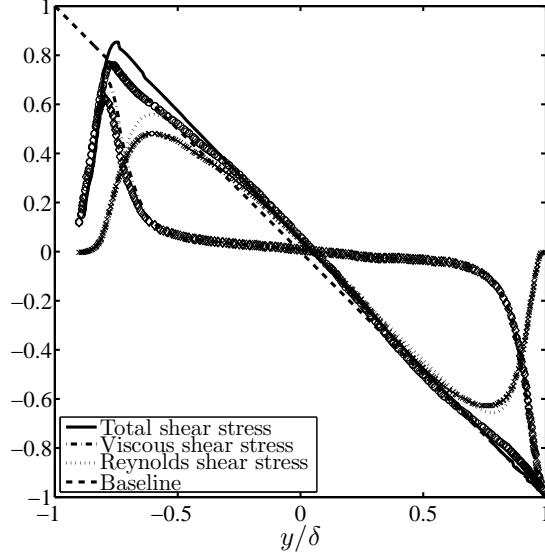
(c)



(d)

For caption see the next page.

tuations and shear stress distribution across the channel at a spanwise location above the riblet mid-point. Note that all profiles are normalized in wall units using the friction velocity of the top (smooth) wall for the ease of comparison. Figure 8 shows the boundary layer profile above the riblet mid-point. In this figure, the von Kármán constant κ and the constant C each has a value of 0.4 [46, 47] and 5.5 [48] respectively in the log-law equation $\bar{u}^+ = \ln y^+ / \kappa + C$ describing the logarithmic layer. Note that the profiles on the riblet wall are computed using the *local* friction velocity for comparison with the reference profiles.



(e)

FIG. 7. Benchmarking of statistics collected from Case II ($l_g^+ \approx 12$) at the riblet mid-point: (a) Mean streamwise velocity profile, (b) Root-mean-square streamwise velocity fluctuations, (c) Root-mean-square wall-normal velocity fluctuations, (d) Root-mean-square spanwise velocity fluctuations, and (e) Shear stress distribution. The profiles are scaled in wall units based on the friction velocity of the top (smooth) wall. The markers (\circ, \diamond, \times) represent the digitized profiles reported by Chu and Karniadakis [25], while the baseline profiles refer to those acquired from the configuration with two plane walls.

The statistics acquired from the baseline plane turbulent channel flow at $Re_m = 1842$ with a same domain size of $5\delta \times 2\delta \times 2\delta$ is also included in the two figures for comparison. Although not shown here, the baseline profiles ($Re_\tau \approx 123$) are comparable with those acquired from a simulation at $Re_\tau \approx 110$ [49].

The profiles for Case II illustrated in figures 7 and 8 are generally in good agreement with those reported by Chu and Karniadakis [25]. However, the profiles of streamwise velocity fluctuations u' between Case II and the reference presented in Fig. 7(b) contain rather significant discrepancy. The peak of the reference profile near the top wall ($y/\delta = 1$) has a lower magnitude than the profiles for Case II and also the baseline configuration. On the other hand, the peak magnitudes of v'_{rms} and w'_{rms} near the top wall reported by Chu and Karniadakis [25] are somewhat higher than the present profiles, and only the profile of v'_{rms} near the riblet wall shows reasonable agreement. Some possible explanations

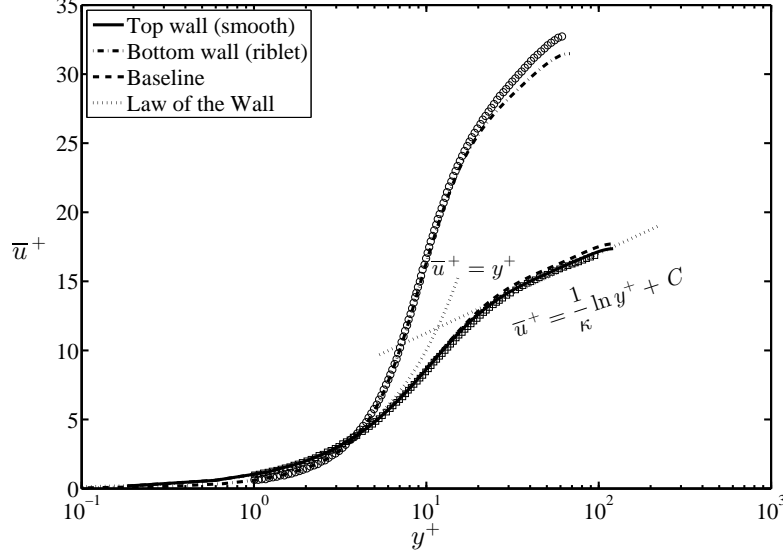


FIG. 8. Boundary layer profile from Case II ($l_g^+ \approx 12$) at the riblet mid-point normalized using the *local* friction velocity ($\kappa = 0.4$ and $C = 5.5$). The marker (\circ, \square) represents the digitized profiles reported by Chu and Karniadakis [25], while the baseline profiles refer to those acquired from the configuration with two smooth walls.

for the discrepancies could be the different mesh resolutions and length of time-averaging. Chu and Karniadakis [25] collected the statistics within 300 non-dimensional time units from a medium resolution mesh which has cross-flow grid spacings of $\Delta y_{min}^+ = 0.42$ and $\Delta z_{min}^+ = 0.43$ near the riblet wall. A study on the effect of mesh resolution in the spectral element framework has shown that the profile of u'_{rms} is under-predicted because of under-resolution in the wall-normal direction [41, p. 475]. On a separate note, simulations of the baseline configuration at $Re_\tau \approx 110$ and 150 [49] revealed that the peak magnitude of u'_{rms} is about 2.6. In this respect, the peak magnitude of u'_{rms} in Case II near the top wall is on a par with the data in the literature, same goes for those associated with v'_{rms} and w'_{rms} .

The comparison of shear stress distributions in Fig. 7(e) also shows some discrepancies, especially near the riblet wall. The peaks of the profiles of Reynolds stress $-\overline{u'v'}^+$ have the largest disparity most likely because of the lower magnitude of u' reported by the reference. On the other hand, a small discrepancy of the peak magnitudes is observed on the profiles of viscous shear stress $\partial \overline{u}^+ / \partial y^+$. In all, these discrepancies lead to a difference in the peak magnitudes of total shear stress near the riblet wall between the present and the reference simulations. Table III summarizes and compares the flow properties between the current

TABLE III. Comparison of flow properties near the smooth (top) and riblet (bottom) walls between the present simulation of Case II and the earlier DNS by Chu and Karniadakis [25]. The riblet spacing and height are $s = 0.2\delta$ and $h = 0.2\delta$ respectively.

	Reference simulation		Present simulation	
	Smooth wall	Riblet wall	Smooth wall	Riblet wall
Re_τ	131	128*	130	128*
$\frac{U_c}{U_m}$	1.22		1.22	
$\frac{U_c}{u_\tau}$	17.08	17.54*	17.25	17.50*
δ^*	0.140	0.205	0.144	0.200
θ	0.079	0.089	0.082	0.085
H	1.77	2.30	1.75	2.34
$G = \frac{U_c}{u_\tau} \left(\frac{H-1}{H} \right)$	7.45	14.85	7.36	14.98
$J = \frac{U_c - U_m}{u_\tau}$	3.08	4.74	3.10	4.70

* Based on the *equivalent* friction velocity averaged over the entire riblet wall.

simulation of V-groove riblets of Case II and the reference [25]. These properties include centerline velocity U_c , friction velocity u_τ , displacement thickness δ^* , momentum thickness θ , shape factor H , Clauser shape parameter G , and velocity defect ratio J . Once again, the decent agreement between the two sets of data ascertains the current simulation setup.

B. Variation of drag reduction performance with the size of riblets

Table IV tabulates the drag reduction performance of all six V-groove riblet configurations. In the same table, the corresponding values of Re_τ , s^+ , h^+ and l_g^+ are also included. Since the smaller computational domain inevitably leads to a higher degree of intermittency in the flow evolution, the percentage drag reduction is calculated by taking the mean value within a reasonable time span towards the end of statistical averaging. In the same way, an uncertainty of $\pm 1\%$ has been estimated with a 95% confidence level. In Case II, the skin friction drag reduction achieved is approximately 4.6%, lower than the approximately 6% reduction reported by the reference DNS. Nonetheless, the experimental results summarized

TABLE IV. Drag reduction performance of V-groove riblets in the channel. The values in wall units are computed based on the surface-averaged friction velocity at the riblet (bottom) wall. Re_τ is the Reynolds number based on the friction velocity on the top (smooth) wall.

Case	s	h	s^+	h^+	l_g^+	Re_τ	ΔDrag (%)
I	0.2δ	0.1δ	20.4	10.2	10.21	125	-5.08
II	0.2δ	0.2δ	17.2	17.2	12.15	130	-4.59
III	0.4δ	0.4δ	43.0	43.0	30.41	137	+35.81
IV	0.2δ	0.1δ	30.6	15.3	15.28	181	+0.79
V	0.2δ	0.2δ	26.9	26.9	19.10	186	+13.86
VI	0.4δ	0.4δ	65.2	65.2	46.15	196	+54.20

by [16] shows 3% to 5% skin friction drag reduction for an identical riblet geometry. Therefore, the current percentage drag reduction falls within the scatter of experimental data. Likewise, García-Mayoral [50] reported a mean drag reduction of 4.32% after reproducing the drag-reducing configuration simulated by Choi *et al.* [20], but with about 18 times longer length of averaging. A separate simulation of Case II with 50% longer domain extent in the two wall-parallel directions produces 3.6% drag reduction and reduces the standard deviation from 0.47% to 0.36%. In view of this, the impact of changing the domain size alone is within the statistical uncertainty. Although the present work has to bear with the slightly larger uncertainty, it is not anticipated to affect the findings or conclusions markedly since the analysis of the six riblet configurations is carried out under similar settings.

Apart from Case II, Case I also yields a drag reduction of 5.1%. However, this configuration with $s^+ \approx 20$ and $h/s = 0.5$ has been shown experimentally by Bechert *et al.* [16] to reduce slightly lesser drag than Case II. The discrepancy is again likely to be caused by the statistical uncertainty. Moreover, the fact that the l_g^+ values of Cases I and II are rather similar, and close to the optimum value, i.e. $l_g^+ \approx 11$ [22] means their performance are difficult to distinguish. On the contrary, the remaining four cases are all drag-increasing configurations. It is observed that the V-groove riblets produce viscous drag reduction only when $l_g^+ \lesssim 15$. This condition is slightly more restrictive than for the thin blade configuration which reduces drag if $l_g^+ \lesssim 17$ [50].

Figure 9(c) illustrates the percentage skin friction drag reduction achieved by the six V-

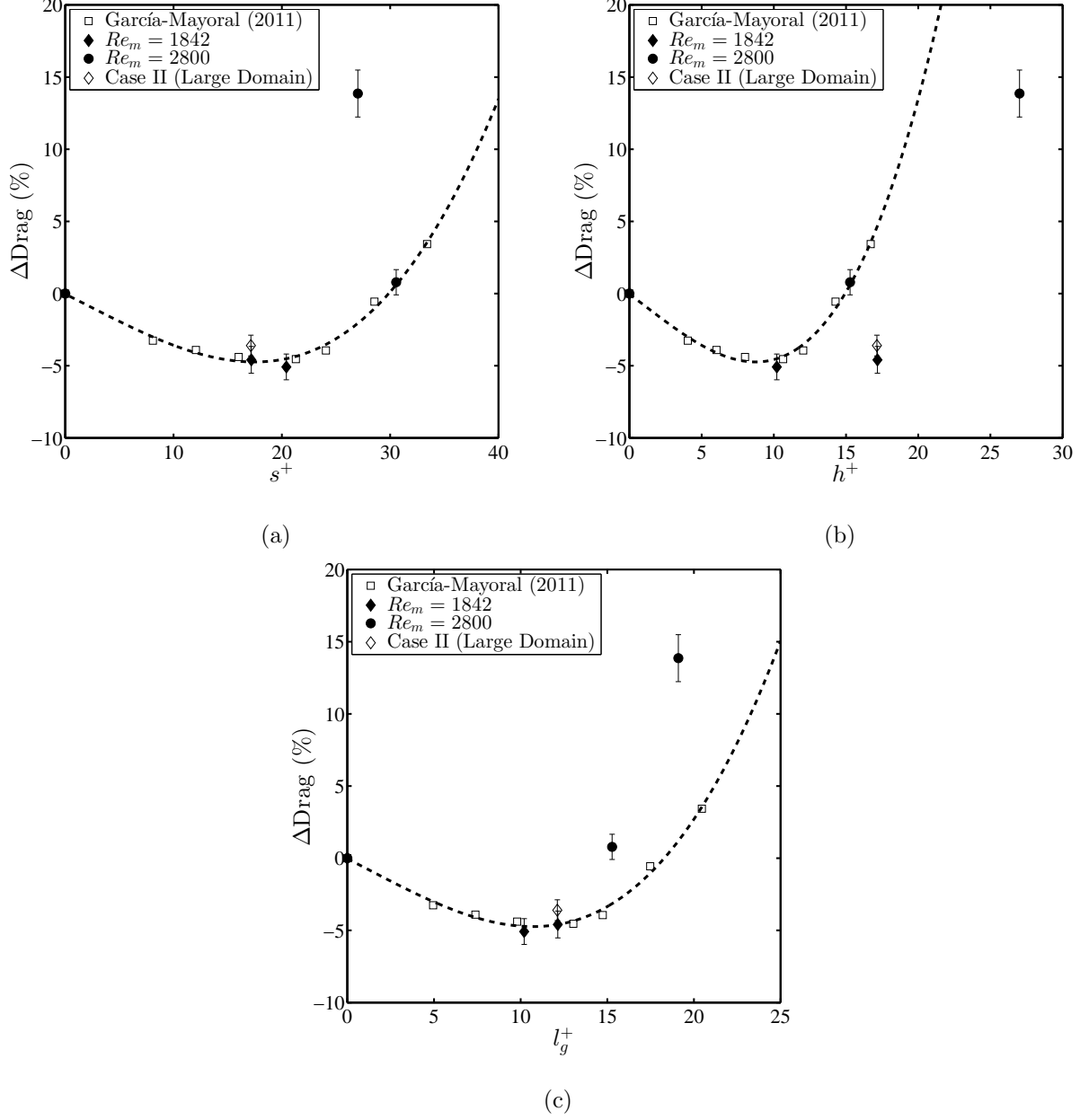


FIG. 9. The scaling of drag reduction curves in terms of (a) s^+ , (b) h^+ , and (c) l_g^+ . Note that the surface-averaged friction velocity on the riblet wall is used to compute the length scale in wall units. The profile for the thin blade riblets reported by García-Mayoral [50] is included. The dash line is a curve-fitted profile of the reference data. The marker (\diamond) is the corresponding value of Case II simulated using a 50% larger domain size. Error bars represent a 95% confidence level.

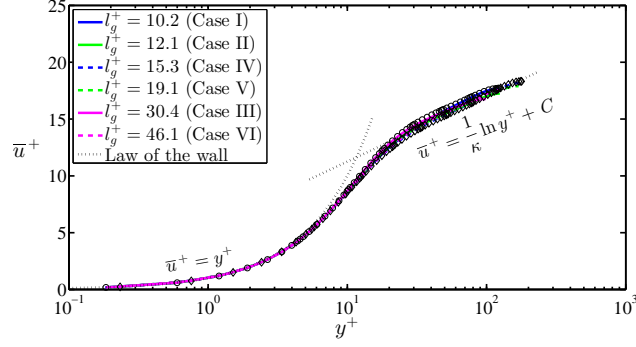
groove riblet configurations against l_g^+ . Note that only those configurations with $l_g^+ < 25$ are shown in the figure, and the error bars represent a 95% confidence level. Also, the baseline turbulent channel flow is assigned a value of $l_g^+ = 0$. The drag reduction curve of the thin

blade riblets reported by García-Mayoral [50] is included to demonstrate the “universality” of the length scale l_g^+ . By comparing Fig. 9(c) with either Fig. 9(a) or 9(b), it is evident that l_g^+ mitigates the dependence on the ratio of h/s . Thus, it offers a better collapse of the data points belonging to the six V-groove configurations. The greatest appeal of l_g^+ is the monotonic variation of the percentage drag reduction, as opposed to the “zig-zag” trend when using either s^+ or h^+ (see also Table IV). In view of this, there is a strong indication that the corresponding flow fields and statistics should also scale monotonically with l_g^+ .

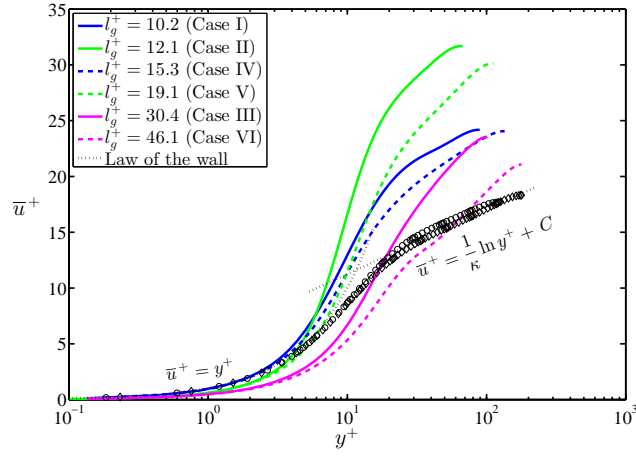
In Fig. 9(c), the agreement with the reference drag reduction curve of thin blade riblets is decent for the cases which have $l_g^+ \approx 10$ and 12, notwithstanding the uncertainty. Although the discrepancy widens with the increase of l_g^+ , García-Mayoral [50] has shown that the data scattering is still significant. One plausible explanation could be the rising importance of inertial effects in the groove due to a greater exposure to the overlying turbulence structures residing in the buffer or logarithmic layers. Alternatively, the breakdown of “universality” may imply that the influence of shape-dependent mechanisms starts to manifest as the local flow transitions from the *viscous* to the *k-roughness* regime. In this respect, it is conjectured that the precise groove geometry becomes an influential factor that dictates the near-wall turbulent motions. One shortcoming of the present work is the lack of data to confirm the fitting in the *viscous regime*, i.e. when $l_g^+ < 10$, because smaller riblets would require even higher mesh resolutions. Nevertheless, the physics of flow in the *viscous regime* has been addressed extensively by Bechert and Bartenwerfer [17], Bechert *et al.* [18], Luchini *et al.* [19], and Grüneberger and Hage [51]. Besides, determining the role of riblet shape in causing the divergent of drag reduction curves when the size of riblets is near or beyond the performance optimum at $l_g^+ \approx 11$ would be more illuminating.

C. Variation of turbulence statistics with the size of riblets

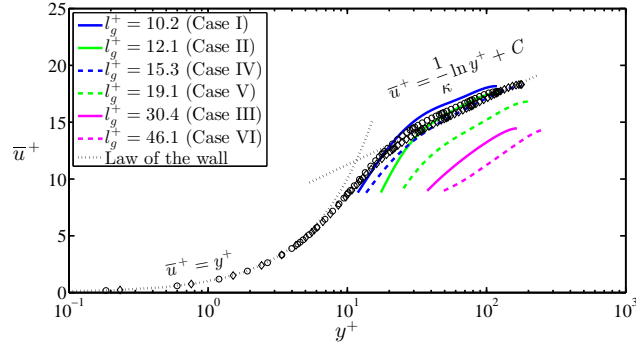
Figure 10 depicts the boundary layer profiles of all six configurations at a spanwise location above the riblet mid-point. Note that the profiles on the riblet wall are computed using the *local* friction velocity. Although the V-groove riblets protrude significantly into the flow, the boundary layer profile on the top smooth wall is hardly affected as seen in Fig. 10(a). In contrast, the boundary layer profile on the riblet surface plotted in wall units using the *local* friction velocity is modified considerably as shown in Fig. 10(b). In Cases III and VI with



(a)



(b)



(c)

FIG. 10. Boundary layer profiles of the six V-groove riblet configurations ($\kappa = 0.4$ and $C = 5.5$): (a) On the smooth top wall (b) Above the riblet mid-point normalized using the *local* friction velocity, and (c) Above the riblet mid-point normalized using the *equivalent* friction velocity. Profiles drawn in solid and dashed lines represent configurations at $Re_m = 1842$ and 2800 , respectively. Likewise, the markers (\circ) and (\diamond) represent the baseline profiles acquired from the configuration with two smooth walls at $Re_m = 1842$ and 2800 , respectively.

$s = h = 0.4\delta$, the inner layer is altered significantly and the log-layer is no longer established with the same slope. On the other hand, significant deviation from the law of the wall is mainly observed on the log-layer for the remaining four riblet configurations with $s = 0.2\delta$. As for the inner layer, the effect is marginal especially for Cases I and III with $h = 0.1\delta$.

In Fig. 10(b), the shifting of the boundary layer profile does not exhibit a clear variation trend with l_g^+ . Instead, the shifting appears to be dependent on the physical dimensions of riblets and/or the bulk Reynolds number Re_m . With the exception of Cases III and VI, the log-layer profile at the same Re_m is shifted upwards with a steeper slope following an increase of the riblet height measured in outer units. In view of this, the threshold value of l_g^+ above which the boundary layer is altered considerably seems to fall in the range $20 < l_g^+ < 30$. Therefore, it is likely that the significant modification of near-wall flow field in these two cases is associated with a different flow feature or mechanism. Interestingly, the riblets in both Cases III and VI have a spacing (see table IV) that is larger than the average diameter of the inherent near-wall streamwise vortices (around 30 wall units). This suggests that the new feature or mechanism could be related to the postulation by Choi *et al.* [20].

Figure 10(c) shows another view of the log-layer profiles on the riblet wall scaled using an *equivalent* friction velocity u_τ^* . u_τ^* is defined as the friction velocity of a plane wall which experiences the same amount of drag as on a riblet wall having an equivalent projected surface area. u_τ^* can also be perceived as the friction velocity averaged over the entire riblet wall. This idea is analogical to computing the friction velocity at the “apparent origin” (see the discussions by McLean [52], p.219-222). Under this alternative normalization, it is clear that the shifting of the log-layer has a direct relation with the drag-reducing ability of the V-groove riblets, and also scales monotonically with l_g^+ . An upward shift is observed in Cases I and II with $l_g^+ < 15$, while a downward shift is observed on the remaining four drag-increasing configurations in which $l_g^+ > 15$. The upward shift in the log-layer or an increase in the intercept C in the log-law equation is a common feature in drag-reduced flows, and it can be perceived as a thickening of the viscous sublayer [20, 53].

Figure 11 depicts the wall-normal distribution of turbulent fluctuations across above the riblet mid-point. The profiles for the baseline configurations with two plane walls at $Re_m = 1842$ and 2800 simulated with the same domain size are also included to illustrate the effects of riblets. Note that all the profiles are scaled in outer units using the bulk streamwise velocity U_m . The rationale of not scaling in wall units is because the friction velocities are

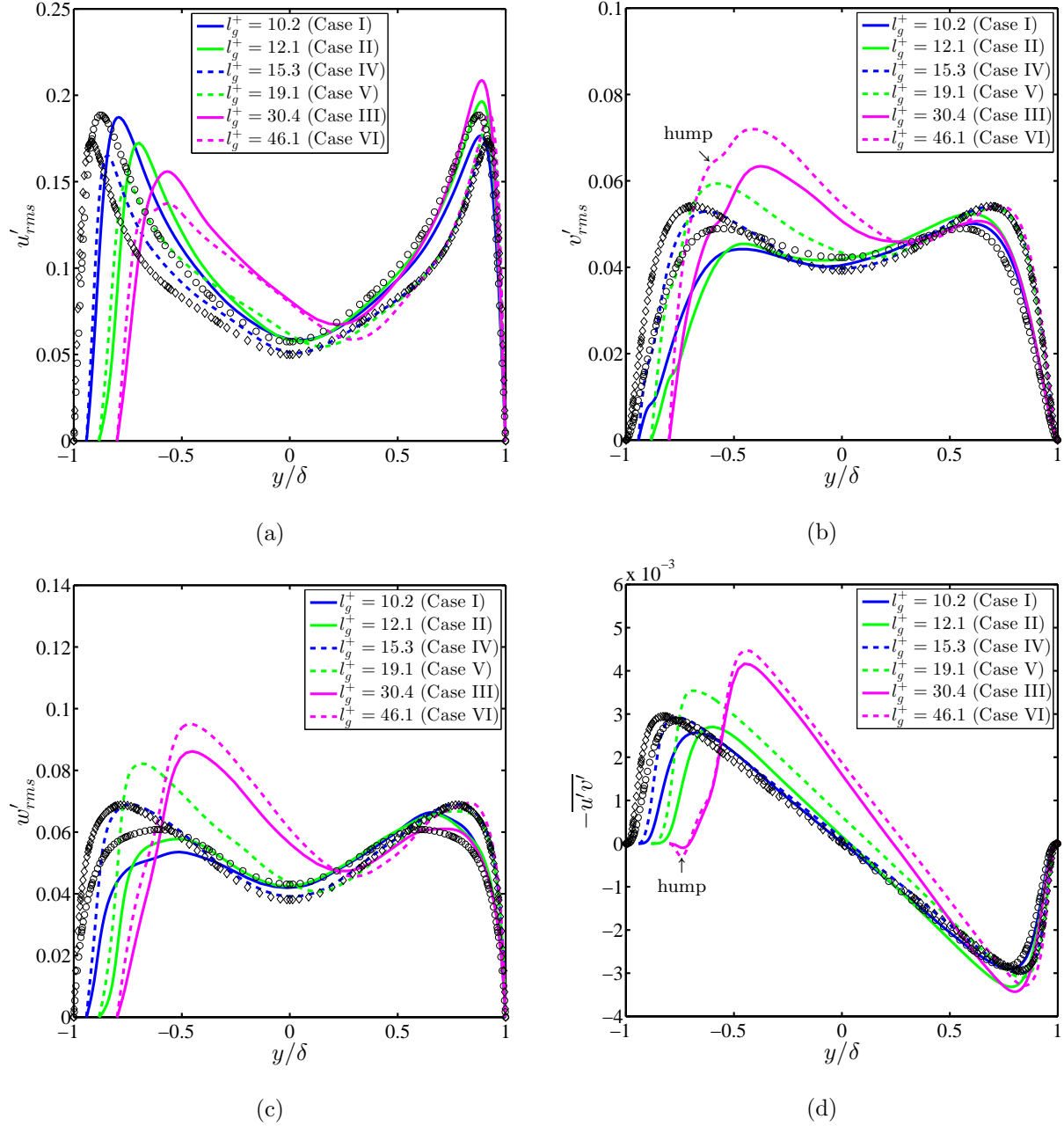


FIG. 11. Profiles of turbulent fluctuations of all six V-groove riblet configurations across the channel above the riblet mid-point: (a) u'_{rms} , (b) v'_{rms} , (c) w'_{rms} , and (d) $-\overline{u'v'}$. Profiles drawn in solid and dashed lines represent configurations at $Re_m = 1842$ and 2800 , respectively. Likewise, the markers (o) and (diamond) represent the baseline profiles acquired from the configuration with two smooth walls at $Re_m = 1842$ and 2800 , respectively. Note that all profiles are scaled in outer units using the bulk velocity U_m .

affected by the different cross-sectional area across the six riblet configurations. Therefore, adhering to the conventional scaling in wall units could yield ambiguous and even misleading comparison, unlike using U_m that is kept the same across all configurations. Furthermore, it is well-known that the profiles of velocity fluctuations do not collapse universally at low Reynolds numbers even when scaled in wall units [54, 55].

In general, the V-groove riblets are able to reduce the peak of streamwise velocity fluctuations u' as compared to the respective baseline configuration. Interestingly, Fig. 11(a) shows that the reduction is proportional to l_g^+ . Furthermore, configurations that have $h/s = 1$ are more effective in reducing the peak of u' , whereas cases I and III with $h/s = 0.5$ have a peak near the riblet wall that is comparable in magnitude to the baseline configuration. The reduction of u' may be attributed to the ability of riblets in aligning the near-wall flow structures thereby manipulating the bursting process [56]. In particular, impeding the lateral motions of near-wall longitudinal vortices leads to premature bursts which in turn give rise to a lower production of turbulence energy [7]. On the other hand, the difference of peaks between the top and bottom walls appears to correlate with the flow asymmetry about the channel centerline, which is observed to be proportional to the riblet height h^+ . Judging from these observations, the impact of riblets on u' may not directly reflect their drag-reducing ability. Instead, the drag reduction performance of V-groove riblets is strongly correlated with the cross-flow velocity fluctuations as illustrated in figures 11(b) and 11(c).

Both Cases I and II which produce a viscous drag reduction exhibit peaks of v' and w' that are discernibly lower than the baseline configuration, and also the corresponding peaks near the top smooth wall. On the contrary, the rest of the drag-increasing cases typically have a higher peaks of v' and w' near the riblet wall. In this respect, a reduction in viscous drag can only be attained when turbulent activities in the cross-flow directions are disrupted. Similarly, a direct relation with the drag reduction performance can be observed from the Reynolds stress profiles shown in Fig. 11(d). This is in line with the conclusions of Fukagata *et al.* [57] and Marusic *et al.* [58] that manipulating the Reynolds stress $-\overline{u'v'}$ is the key to achieve effective control of wall turbulence and substantial viscous drag reduction. More astonishingly, one can see that the peaks of the cross-flow velocity fluctuations and Reynolds stress near the riblet wall also scale monotonically with l_g^+ .

Figure 12 shows the percentage change in the peak magnitudes of v'_{rms} , w'_{rms} and $-\overline{u'v'}$ above the riblet mid-point plotted against l_g^+ . In Fig. 12(a), the percentage change is com-

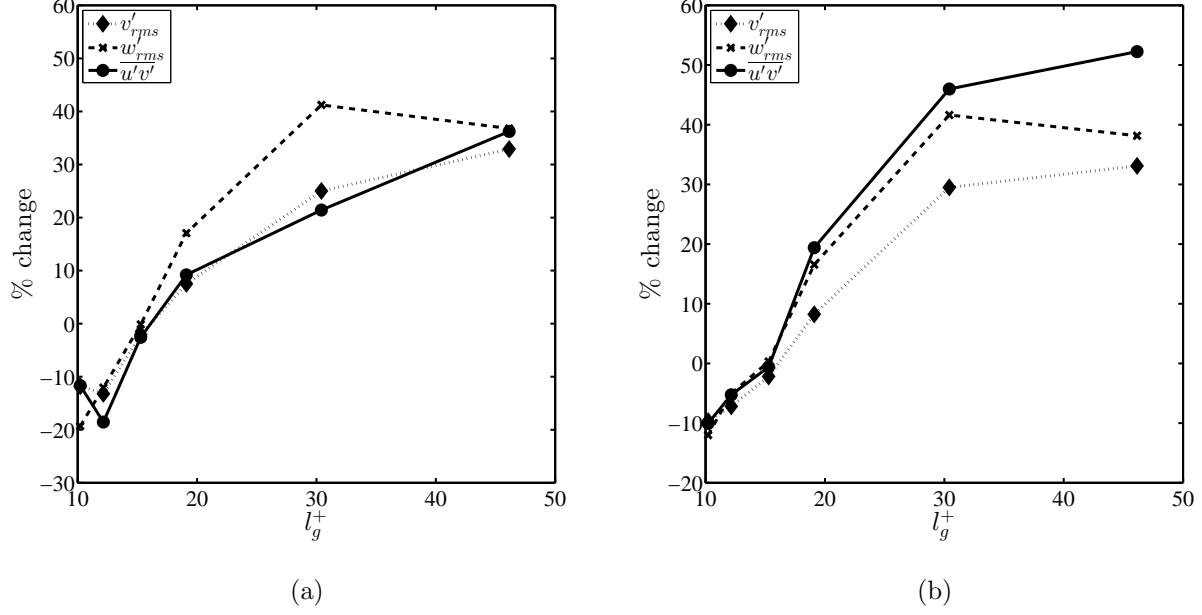


FIG. 12. Percentage change of the peak magnitudes of v'_{rms} , w'_{rms} and $-\overline{u'v'}$ of the six riblet configurations above the riblet mid-point as a function of l_g^+ : (a) Computed with respect to the top (smooth) wall, and (b) Computed with respect to the baseline configuration.

puted with respect to the top smooth wall and it shows a positive correlation with l_g^+ in general. The same trend is observed in Fig. 12(b) when computed with respect to the baseline configuration. A small deviation from the trend is mainly observed in Fig. 12 on the profiles of v'_{rms} and $-\overline{u'v'}$ at $l_g^+ \approx 10$ and 12. The reason could be because the performance and statistics are rather difficult to distinguish given the close proximity in riblet size. Moreover, these two configurations also have different ratios of h/s which means they experience different degree of flow asymmetry about the centerline.

Interestingly, the profiles in Fig. 12(b) exhibit a somewhat linear trend and a rather decent collapse when $10 < l_g^+ < 16$, i.e. Cases I, II and IV. This trend seems to imply that the rise in Reynolds stress goes hand in hand with the augmentation of cross-flow velocity fluctuations v' and w' . In this regard, the changes of v' , w' and $-\overline{u'v'}$ may be caused by similar mechanism. As l_g^+ gets larger than 16 (or $s^+ > 30$), the profiles start to diverge and the Reynolds stress increases at a greater magnitude, followed by the spanwise and then the wall-normal velocity fluctuations. Such behavior indicates that there are additional mechanisms associated with the cross-flow that come into play as the groove size becomes larger. Moreover, the fact that the peak magnitude of u' is reduced while those of v' and

w' are augmented suggests that the increasing reach of riblets in the bulk flow induces a transfer of energy from the streamwise to the cross-flow components of velocity fluctuations. Previously, Choi *et al.* [20] (figure 18 in their paper) showed that V-groove riblets at $s^+ = 40$ produced a considerable spanwise variation of the peaks of turbulence kinetic energy k , in which the maximum occurred at the riblet tip. Hence, it may not be surprising that larger riblets exhibit additional flow features or mechanisms centering about the tip.

One interesting observation in Fig. 11(b) is that the profiles of v'_{rms} of all the six riblet configurations feature a small hump at a level around the riblet tips. This seems to be a sign of turbulence activities happening close to the tips since no discernible hump is found on the corresponding profiles above the riblet valley, see Fig. 13(b). The appearance of hump may be attributed to the shedding of vortices due to the sharp tip of V-groove riblets as speculated by Goldstein *et al.* [59]. Judging from the present results, the appearance of hump seems to be a ubiquitous feature in flows over V-groove riblets that is independent of the riblet size. The hump feature on the profile of v'_{rms} could also be perceived as a testament to the ability of riblets in aligning the flow structures, or in localizing the overlying streamwise vortices above the riblet grooves as reported by García-Mayoral and Jiménez [22].

Although no hump is formed on the profiles of v'_{rms} above the riblet valley, humps are found on the profiles of u'_{rms} depicted in Fig. 13(a). However, the humps are formed in regions within the groove, and only for riblet configurations with $h/s = 1$, i.e. except Cases I and IV. Similar kind of hump feature on the profiles of u'_{rms} above the riblet valley has been reported by Chu and Karniadakis [25], while Choi *et al.* [20] and Goldstein *et al.* [59] did not observe any formation of humps from their simulations of V-groove riblets. Nonetheless, Goldstein *et al.* [59] speculated that such feature is related to the shedding of vortices by the pointed riblet tip, but they concluded that the presence and importance of the hump remains an open question. A forthcoming study will show that such phenomenon occurring in the groove can be explained by looking at the flow topology on the riblet wall, and that its nature is dictated by the groove shape.

Apart from the humps found on the profiles of u'_{rms} above the riblet valley, Fig. 13(d) reveals that humps also appear on the profiles of $-\overline{u'v'}$ belonging to Cases V, III and VI with $l_g^+ \approx 19, 30$ and 46 , respectively. The hump is formed more prominently as l_g^+ increases. In particular, the hump in Case VI is formed deeper in the groove than in Case III despite they share the same physical riblet height $h = 0.4\delta$. A similar hump is also observed in Fig. 13(a)

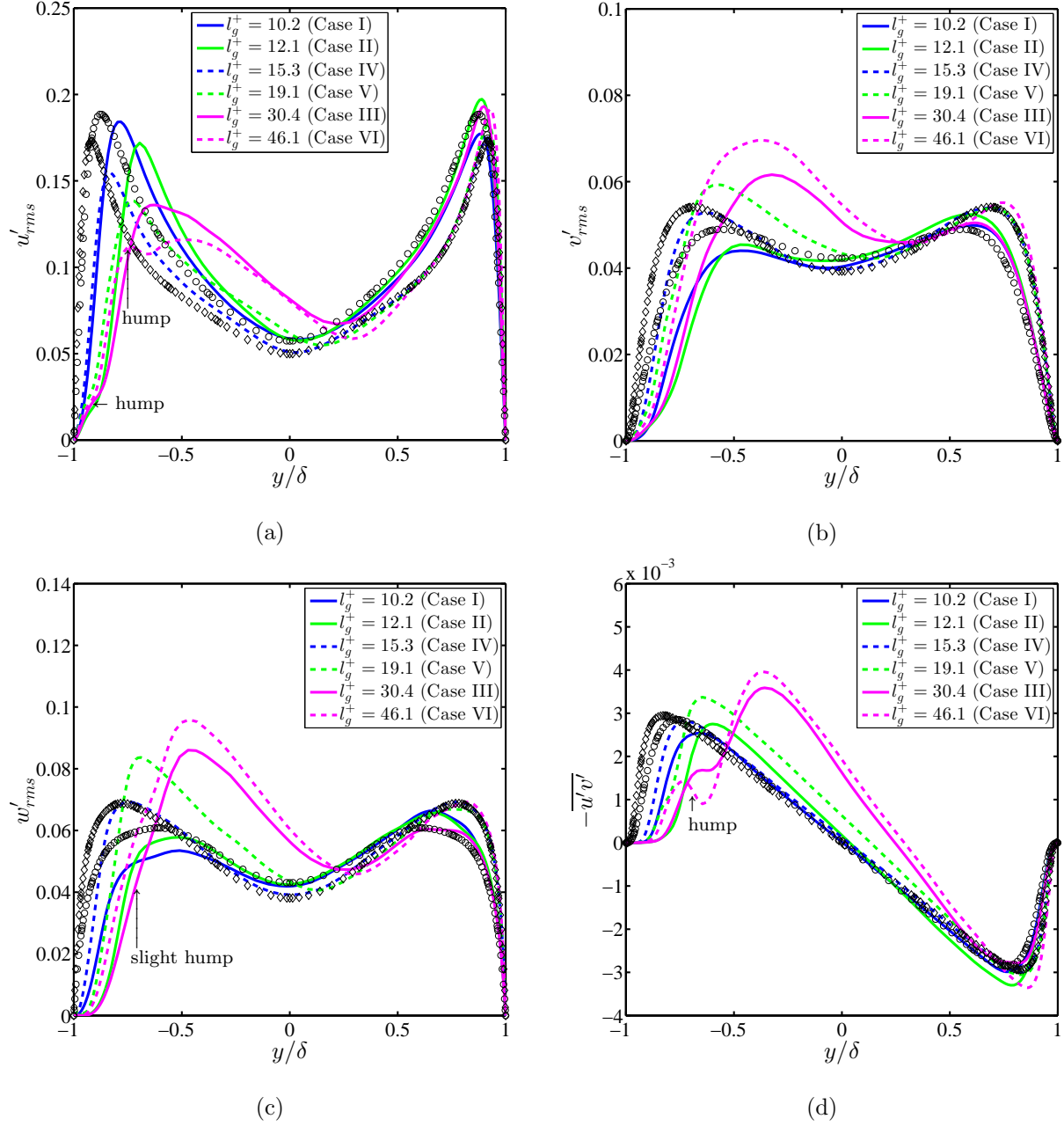


FIG. 13. Profiles of turbulent fluctuations of all six V-groove riblet configurations across the channel above the riblet valley: (a) u'_{rms} , (b) v'_{rms} , (c) w'_{rms} , and (d) $-\overline{u'v'}$. Profiles drawn in solid and dashed lines represent configurations at $Re_m = 1842$ and 2800 , respectively. Likewise, the markers (\circ) and (\diamond) represent the baseline profiles acquired from the configuration with two smooth walls at $Re_m = 1842$ and 2800 , respectively. Note that all profiles are scaled in outer units using the bulk velocity U_m .

on the profile of u'_{rms} for Case VI at roughly the same wall-normal distance away from the riblet valley. On the other hand, a peculiar feature in Fig. 11(d) is the small hump on the profile of Case VI at $y/\delta \approx -0.7$ which indicates a negative contribution to the Reynolds stress. Similarly, a small dip is also observed on the corresponding profile of Case III. In other words, when l_g^+ gets sufficiently large, the flow field in some part the groove can become slightly dominated by $Q1$ and $Q3$ motions as opposed to the typical $Q2$ (*ejection*) and $Q4$ (*sweep*) motions based on the idea of *quadrant analysis* [60]. The above discussions point to the fact that the flow field in the vicinity of V-groove riblets becomes increasingly complex when their size gets sufficiently large, i.e. when $l_g^+ > 15$ based on the present set of configurations. This condition also corresponds with the divergent of profiles in Fig. 12(b).

Similar arguments can be derived when analyzing the corresponding profiles of turbulence fluctuations above the riblet tip provided in Fig. 14, except for a few differences in Cases III and VI that possess the two largest values of l_g^+ . Firstly, it is observed that the peak magnitude of u' near the riblet wall is comparable to the baseline configuration. They are found to augment the peak magnitude of u' when their size becomes too large, i.e. at $l_g^+ \approx 30$ and 46. Although the attenuation of the peak magnitude of u' still scales with l_g^+ , the V-groove riblets are less effective in mitigating the peak magnitude of u' directly above the riblet tip. Secondly, humps are formed on the profile of w'_{rms} near the riblet tip at $y/\delta \approx -0.6$. Both of these findings suggest that u' and w' are intensified at the tip when the size of riblets is large. On the other hand, there are no humps formed on the profiles of v' and $-\overline{u'v'}$ as opposed to those plotted above the riblet mid-point and valley. However, the peak magnitude of $-\overline{u'v'}$ is noticeably higher, especially in those configurations with $l_g^+ > 15$.

D. Variation of flow features with the size of riblets

Previously, Choi *et al.* [20], Lee and Lee [61], and El-Samni *et al.* [62] have concluded that the skin friction drag is augmented when near-wall streamwise vortices penetrate into the groove if $s^+ > 30$, and vice-versa. Based on the present set of riblet configurations, both Cases III and VI possess $s^+ > 30$, thereby exceeds the condition specified by Choi *et al.* [20]. Figures 15 and 16 compare, respectively, the instantaneous streamlines pattern and streamwise vorticity ω_x contours of the six configurations on a cross-sectional plane at $x/\delta = 2.5$. These figures show that the behavior of near-wall vortical structures somewhat

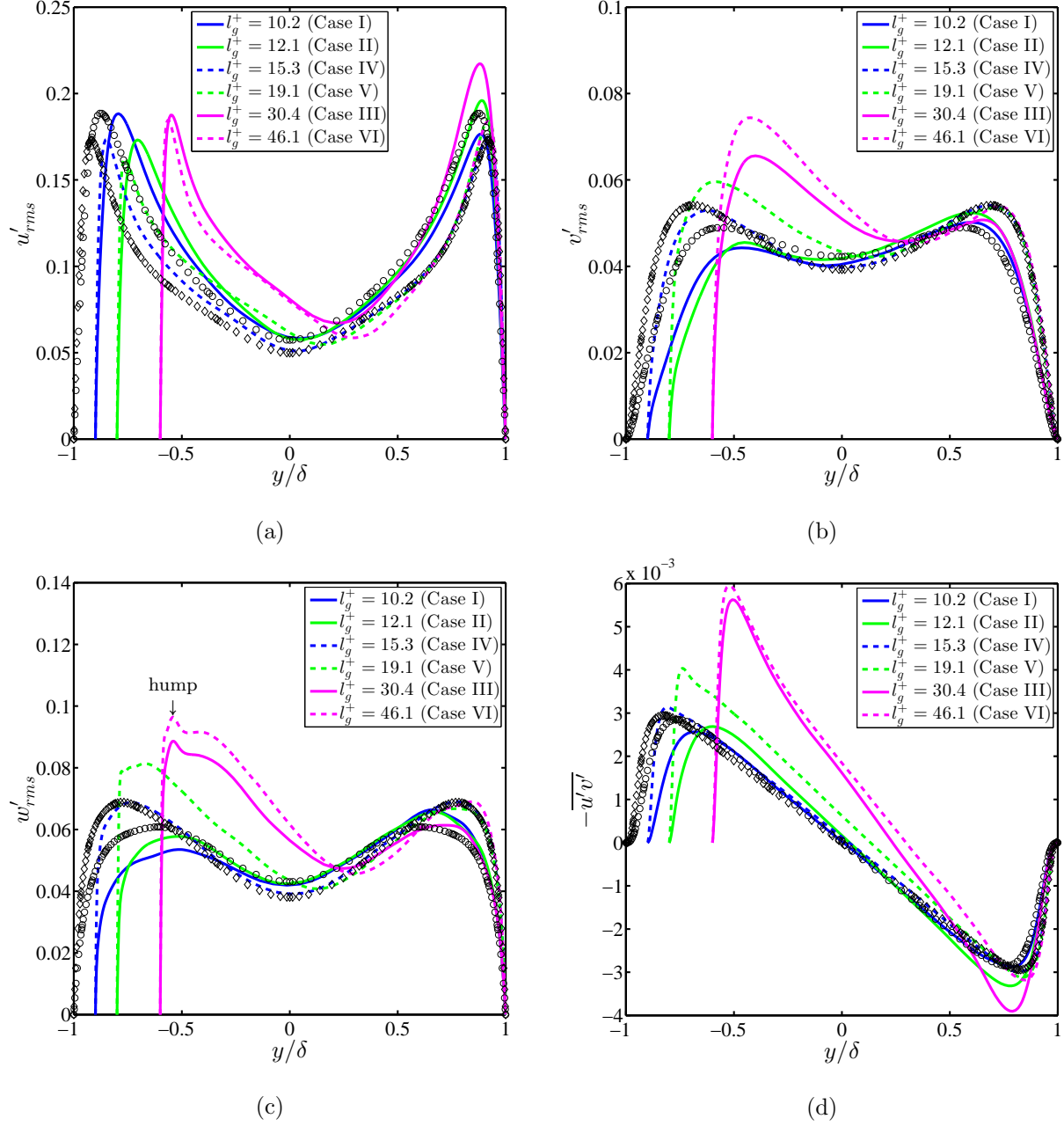


FIG. 14. Profiles of turbulent fluctuations of all six V-groove riblet configurations across the channel above the riblet tip: (a) u'_{rms} , (b) v'_{rms} , (c) w'_{rms} , and (d) $-\overline{u'v'}$. Profiles drawn in solid and dashed lines represent configurations at $Re_m = 1842$ and 2800 , respectively. Likewise, the markers (\circ) and (\diamond) represent the baseline profiles acquired from the configuration with two smooth walls at $Re_m = 1842$ and 2800 , respectively. Note that all profiles are scaled in outer units using the bulk velocity U_m .

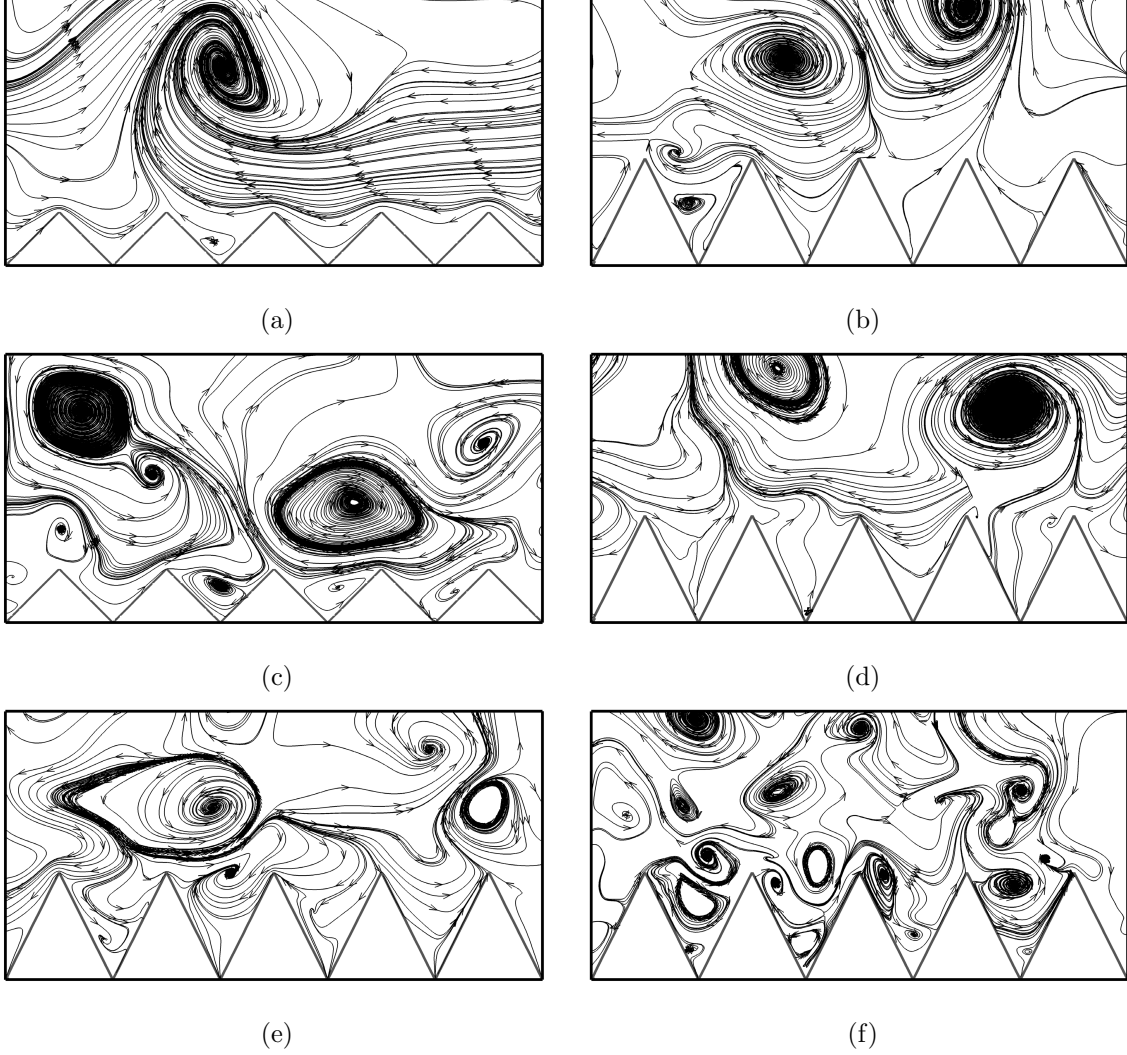


FIG. 15. Comparison of instantaneous near-wall streamlines pattern on a yz -plane at $x/\delta = 2.5$ of the six riblet configurations near the riblet wall: (a) $l_g^+ \approx 10$ (Case I), (b) $l_g^+ \approx 12$ (Case II), (c) $l_g^+ \approx 15$ (Case IV), (d) $l_g^+ \approx 19$ (Case V), (e) $l_g^+ \approx 30$ (Case III), and (f) $l_g^+ \approx 46$ (Case VI). Note that the figures are rescaled to visually the same riblet spacing s/δ for comparison purpose.

scales with l_g^+ . Note that the visualizations for the riblet walls have been rescaled to visually the same spacing in both sets of figures. It is worthwhile to mention that the vortical regions identified by the streamlines and vorticity contours may not match entirely because the near-wall streamwise vortices are continuously shifting their positions with time [63].

In Cases I and II, the average size vortices have a tendency to stay above the riblets. Figure 16 reveals that the bulk of the groove is free from vortical fluid motions. Thus, a small reduction in the peak magnitudes of cross-flow velocity fluctuations v' and w' is

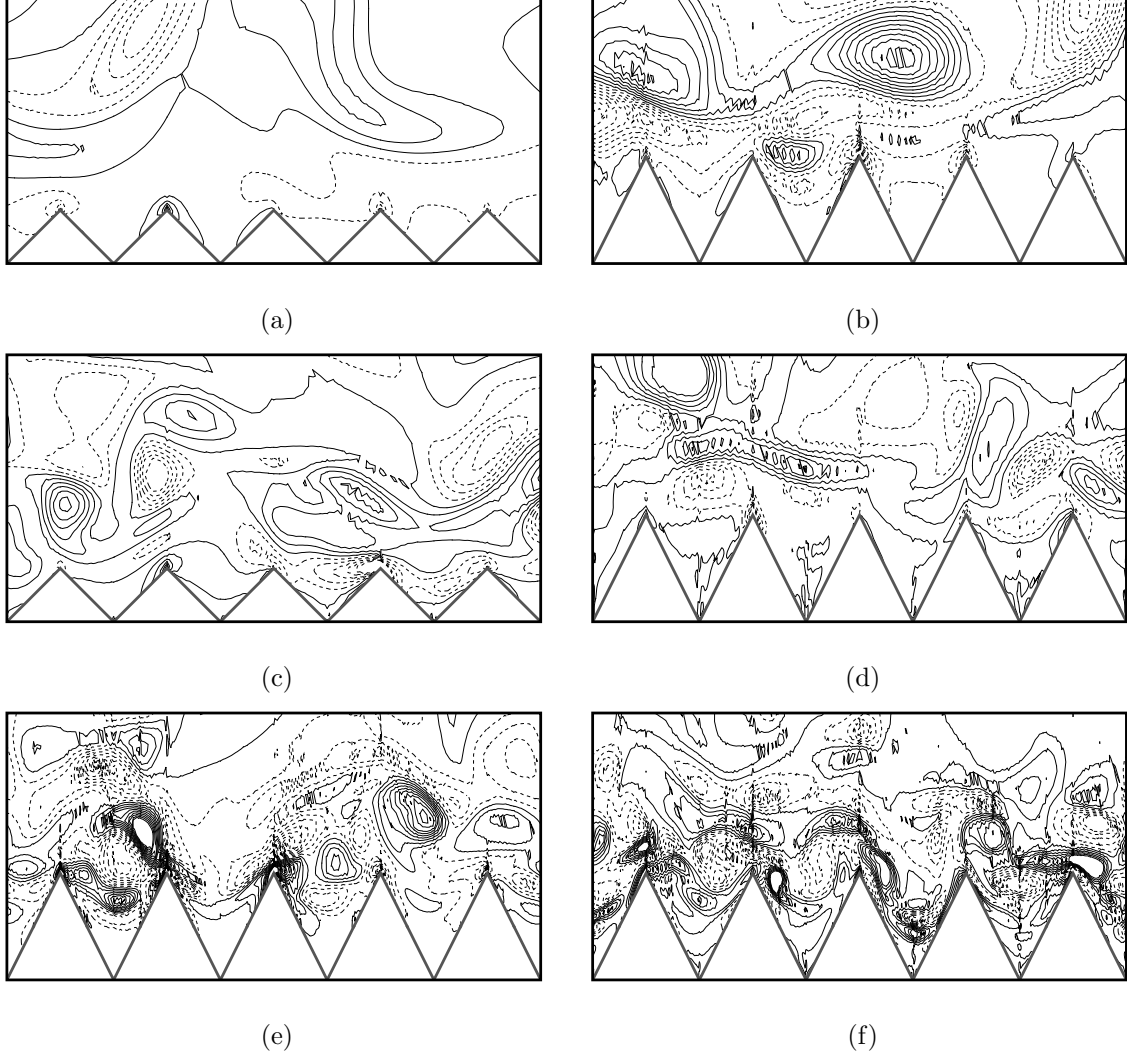


FIG. 16. Comparison of instantaneous near-wall streamwise vorticity ω_x pattern on a yz -plane at $x/\delta = 2.5$, between the top (smooth) wall and the bottom (riblet) wall: (a) $l_g^+ \approx 10$ (Case I), (b) $l_g^+ \approx 12$ (Case II), (c) $l_g^+ \approx 15$ (Case IV), (d) $l_g^+ \approx 19$ (Case V), (e) $l_g^+ \approx 30$ (Case III), and (f) $l_g^+ \approx 46$ (Case VI). Note that the flow is into the plane ($+x$ direction), and dashed lines indicate negative vorticity (counterclockwise rotation). All the figures have the same number of contour levels evenly distributed within the same range, and they are rescaled to visually the same riblet spacing s/δ for comparison purpose.

achieved in these two cases. The analysis by García-Mayoral and Jiménez [22] also arrived at the same conclusion that the lodging of vortices inside the grooves does not happen in the neighborhood of performance optimum, i.e. around $l_g^+ \approx 11$. As l_g^+ gets larger, there are increasingly more vortical structures that reside in the groove. As seen in Fig. 16, there

are more distinct vortical regions in the groove when $l_g^+ > 30$, and these regions penetrate deeper into the groove as l_g^+ increases to 46. As a result, these lodged vortices interact more frequently, and with a larger extent of the groove surface. In this regard, a notable rise of turbulent fluctuations would be expected, and it is reflected on the flow statistics presented in the preceding section. In addition, it is likely that the mutual interactions among the vortices are invigorated because of being confined within the groove, and all along subjected to the strong non-linear inertial effects exerted by the overlying flow structures. Naturally, the more complex and energetic turbulent motions would augment the friction drag significantly.

One can also relate the intensified turbulent motions to the appearance of a second peak on the profile of $-\overline{u'v'}$ for Cases III and VI as shown in figures 11(d) and 13(d). The same goes for the hump that formed on the profile of u'_{rms} for Case VI, see figure 13(a). On the other hand, the fact that discernible humps are only formed on the profiles of w'_{rms} above the tip demonstrates that riblets are still rather effective in impeding spanwise turbulent motions in the groove. However, Fig. 13(c) reveals that there is a marginal enhancement of w'_{rms} in the groove in Cases III and VI with $l_g^+ > 30$, which manifest as a slight hump on the statistical profiles. Although there are strong indications that the lodging of vortices lead to intensified, and dynamically complex near-wall turbulent motions, its implications on the viscous drag cannot be established definitively. One would have to isolate and study the impact of their actions around riblets under a controlled setting.

Figure 17 presents the contours of streamwise component of time-averaged vorticity $\overline{\omega}_x$ of the six configurations to look at the impact of increasing l_g^+ on the mean secondary flow. The first observation is that the strength of the secondary vorticity indicated by the density of the contours increases with l_g^+ . In particular, it strengthens drastically when l_g^+ transitions from 15 to 19, which coincides with the divergent of the profiles depicted in Fig. 12(b). Secondly, the secondary flow also tends to reach deeper into the groove as l_g^+ increases. As the secondary flow appears to draw high momentum fluid from the core region towards the riblet valley, it could cause the instantaneous lodging of near-wall flow structures in the groove. In this regard, it can be postulated that the increasingly complex near-wall fluid motions that begins when $l_g^+ > 15$ are associated with the strengthening of the mean secondary flow. In turn, these phenomena seem to correlate with the higher viscous drag.

Figure 18 depicts the distribution of $-\overline{u'v'}$ around the six configurations of riblets. One can

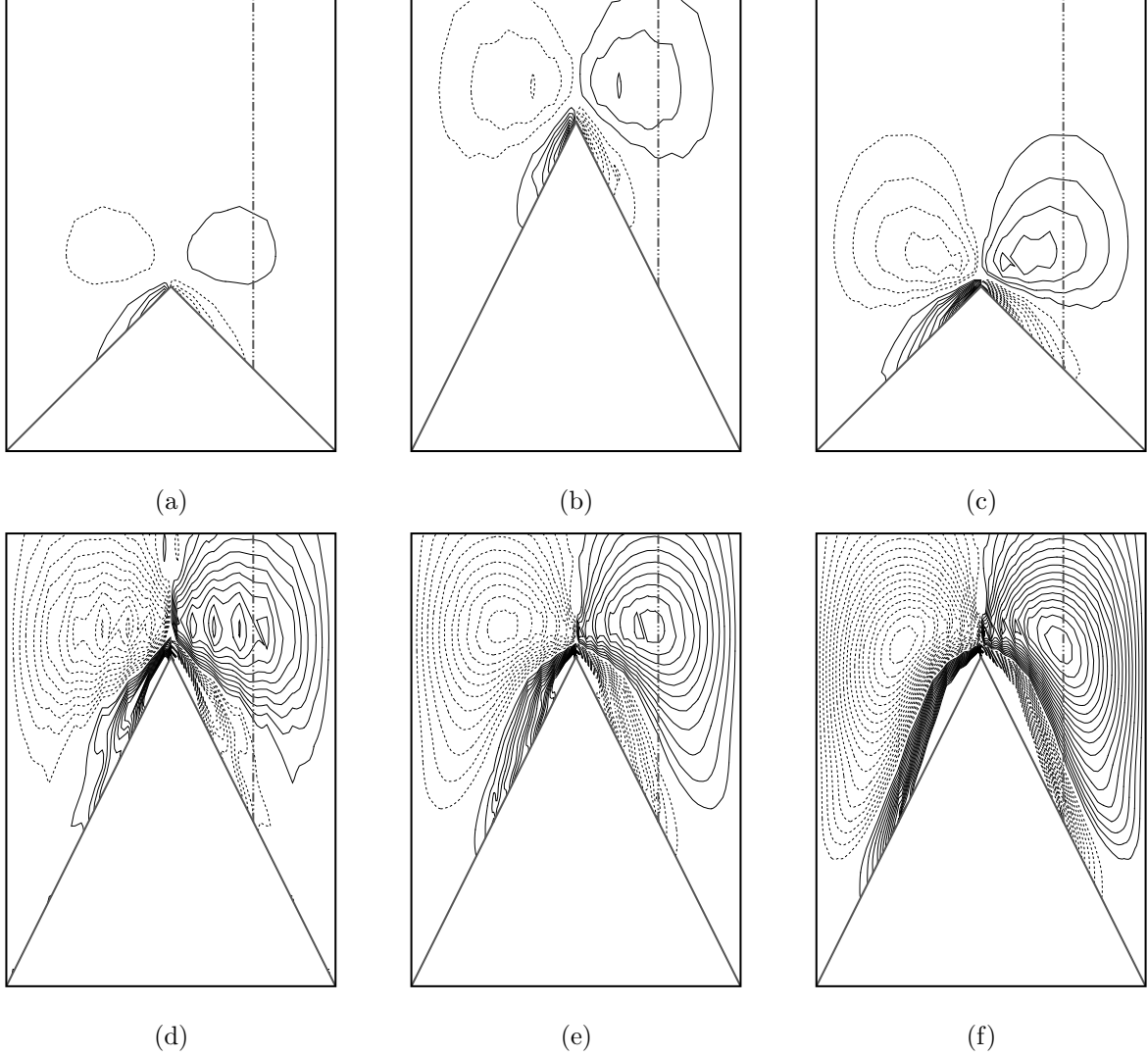


FIG. 17. Comparison of near-wall time-averaged streamwise vorticity contour $\bar{\omega}_x$ near the bottom (riblet) wall: (a) $l_g^+ \approx 10$ (Case I), (b) $l_g^+ \approx 12$ (Case II), (c) $l_g^+ \approx 15$ (Case IV), (d) $l_g^+ \approx 19$ (Case V), (e) $l_g^+ \approx 30$ (Case III), and (f) $l_g^+ \approx 46$ (Case VI). Note that dashed lines indicate negative vorticity (counterclockwise rotation). Figures are rescaled to visually the same riblet spacing s/δ for comparison purpose, and the contours have the same number of levels and range. The vertical lines (— -- —) indicate the riblet mid-point.

see that a sign change of $-\overline{u'v'}$, demarcated by the dashed contour lines, occurs in both Cases III ($l_g^+ \approx 30$) and VI ($l_g^+ \approx 46$). Hence, the humps on the corresponding statistical profiles depicted in Fig. 11(d) are the manifestation of such region since it lies in the proximity of the riblet mid-point where the profiles are extracted. A comparison between figures 17 and 18 shows that such region is found along the boundary where the mean secondary flow

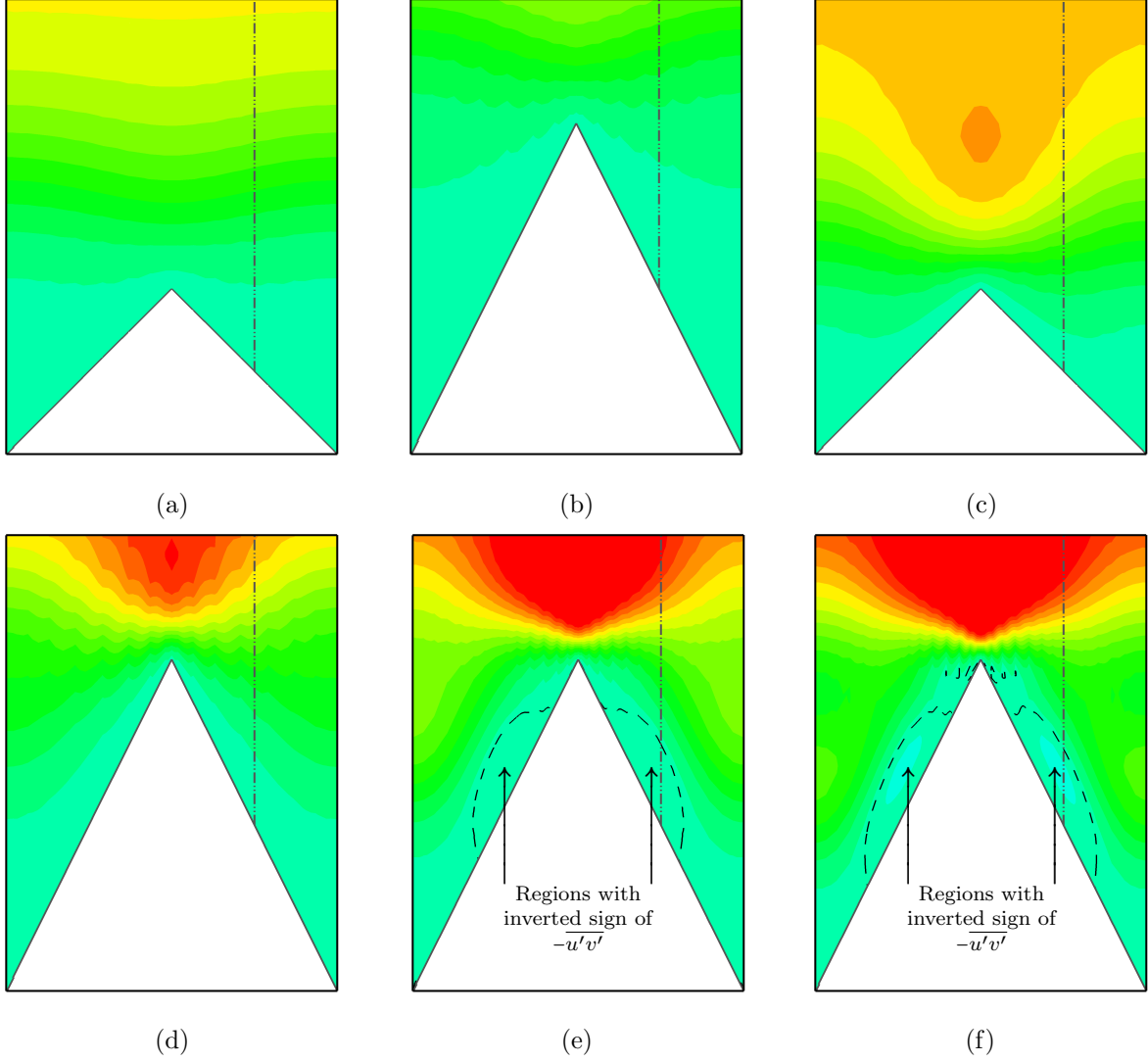


FIG. 18. Comparison of time-averaged Reynolds shear stress $-\overline{u'v'}$ near the bottom (riblet) wall: (a) $l_g^+ \approx 10$ (Case I), (b) $l_g^+ \approx 12$ (Case II), (c) $l_g^+ \approx 15$ (Case IV), (d) $l_g^+ \approx 19$ (Case V), (e) $l_g^+ \approx 30$ (Case III), and (f) $l_g^+ \approx 46$ (Case VI). Figures are rescaled to visually the same riblet spacing s/δ for comparison purpose, and the contours have the same number of levels and range. The vertical lines (---) indicate the riblet mid-point, whereas the contour lines (---) demarcate the level of $-\overline{u'v'} = 0$.

meets the opposing vortex induced on the riblet surface. Furthermore, the region penetrates deeper into the groove and its magnitude becomes larger as l_g^+ increases from 30 to 46. Both features suggest that the sign inversion is associated with the induced mean secondary flow. In an earlier work, Crawford and Karniadakis [64] showed that the spanwise variation of the Reynolds stress component $-\overline{u'w'}$ can modify the gradient of $-\overline{u'v'}$, and the sign of $\partial \overline{u'w'}/\partial z$

has a direct connection with the wall-normal transport of fluid by the secondary flow.

Goldstein and Tuan [21] conjectured that the generation of secondary flow involves spanwise sloshing of the flow near the riblet elements due to the presence of spanwise velocity fluctuations w' having a range of frequencies and amplitudes. Indeed, a recap of Fig. 12(b) reveals that the peak magnitude of w'_{rms} increases at a greater extent than the one in the wall-normal direction when $l_g^+ > 15$. One plausible explanation could be that larger riblets become less effective in impeding the lateral motions of near-wall flow structures. Moreover, since the groove spacings for Cases IV, III and VI (see table IV) all of which with $l_g^+ \gtrsim 15$ are larger than 30 wall units, the lateral motions near-wall flow structures could be promoted rather than mitigated while they are evolving and mutually interacting over riblets. A related conjecture is that larger riblets give rise to stronger spanwise variation of the near-wall flow field, and it in turn leads to force imbalance that can induce cross-flow motions.

E. Additional correlations with the size of riblets

Apart from serving as a means to characterize the drag reduction performance, the present work intends to explore the potential of l_g^+ in correlating the changes of other interesting flow properties with the size of riblets. Of particular interest is whether there exists a connection between the riblet size defined in terms of l_g^+ and the overall turbulent flow field in the channel. In earlier works, it was postulated that mitigating Reynolds stresses could result in a significant skin friction drag reduction [57]. Likewise, it has been demonstrated that the skin friction drag is predominantly contributed by the Reynolds stresses in flows at high Reynolds number [65]. As such, the present study would like to examine the implications of riblets on the fluctuating velocity field in the light of l_g^+ .

Based on an energy consideration of the fluctuating velocity field, Marusic *et al.* [58] showed that the criterion for achieving sustained sub-laminar drag in a channel flow with a fixed volume flux is equivalent to exceeding the volume flux of laminar flow in a channel flow driven by a fixed pressure gradient. The criterion is given as:

$$\Gamma > \langle |\nabla \mathbf{u}|^2 \rangle + Re_m^2 \left\langle \left[\overline{u'v'} - \langle \overline{u'v'} \rangle \right]^2 \right\rangle \quad (3)$$

where Γ is a parameter related to the choice of control scheme. The overbar denotes averaging in time and along the homogeneous directions. $\langle \rangle$ denotes bulk averaging over the

channel cross-section. \mathbf{u} is the velocity fluctuations vector. Note that all flow quantities in expression (3) have been normalized accordingly by the length scale δ and velocity scale U_m .

Let us denote the right hand side of expression (3) as Γ^* . In its original derivation, Γ^* denotes the threshold for blowing or suction techniques to achieve sustainable sub-laminar drag in a channel flow. The larger is the value of Γ^* , the more difficult it is to damp out the turbulent stresses [58]. In the present context, this parameter can thus be employed to quantify the state of turbulence in the presence of riblets, which is predominantly influenced by the quantity $-\overline{u'v'}$. Such effect is captured by the second term on the right hand side of equation (3). Although there is an additional non-zero component of Reynolds stresses, i.e. $-\overline{u'w'}$, due to the spanwise inhomogeneity near the riblet wall, its net effect is nullify after taking a bulk-averaged of the flow field because of the symmetry of V-groove riblets.

Figure 19(a) shows the profiles of Γ^* against l_g^+ . Firstly, the baseline value of Γ^* at $Re_m = 2800$ is greater than the one at $Re_m = 1842$. This is consistent with a more chaotic flow field at higher Reynolds numbers. Note that the baseline configurations mentioned here are simulated with a domain size of $5\delta \times 2\delta \times 2\delta$ to be consistent with the riblet configurations. It is found that the variations of both percentage drag reduction and Γ^* of all the six simulated riblet configurations follow the same trend. For the cases where $l_g^+ \approx 10$ and 12, both representing the drag-reducing configurations, the values of Γ^* are lower than the baseline value. On the contrary, the rest of the drag-increasing configurations have values of Γ^* that are greater than the corresponding baseline values. The similar trend confirms that any attempt to reduce the viscous drag would have to involve the manipulation of $\overline{u'v'}$.

However, it is noted that the computed percentage drag reduction at $l_g^+ \approx 10$ is greater than the one at $l_g^+ \approx 12$. The lower Γ^* value in Case II is not surprising given that the mitigation of u' is more effective when $h/s = 1$, and Case II should reduce slightly greater drag according to experimental measurements [16]. In addition, the percentage drag reduction is subjected to an uncertainty of $\pm 1\%$. Disregarding this slight anomaly, Γ^* could serve as an alternative indicator of the effectiveness of different riblet configurations in manipulating the state of turbulence in a channel flow.

Next, a parameter \mathcal{D} involving the mean velocity gradient or deformation tensor is defined:

$$\mathcal{D} = \left\langle |\nabla \overline{\mathbf{V}}|^2 \right\rangle \quad (4)$$

This quantity provides an indication of the degree of deformation in the mean flow. It can

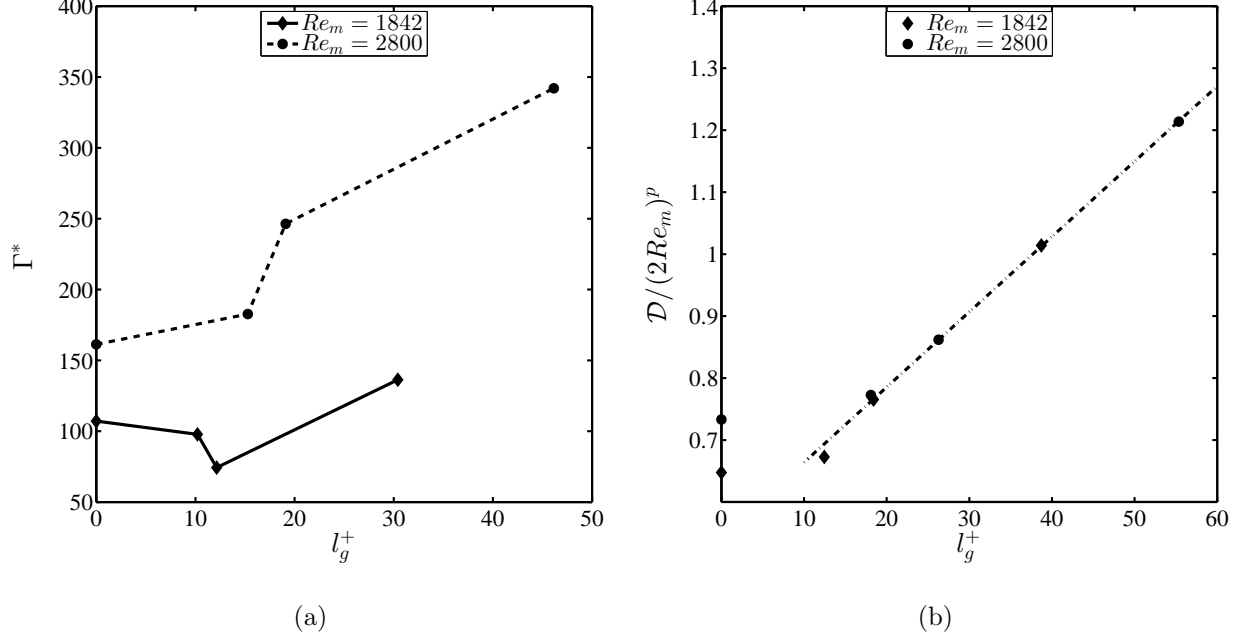


FIG. 19. (a) Profiles of Γ^* against l_g^+ , and (b) Profiles of $\mathcal{D}/(Re_m)^p$, where $p = 0.26$, against l_g^+ . Note that the values of l_g^+ in Fig. 19(b) are computed based on the surface-averaged friction velocity on the smooth (top) wall.

be perceived as a quantity related to the energy dissipation of the mean flow by viscosity. Figure 19(b) shows a graphical view of \mathcal{D} normalized by a power law of the Reynolds number, i.e. $(Re_m)^p$, where $p = 0.26$. In this case, values of l_g^+ are computed using the surface-averaged friction velocity on the smooth (top) wall. The curves at two distinct Reynolds numbers appear to collapse onto a single curve under such normalization. Figure 19(b) also illustrates that \mathcal{D} is linearly proportional to l_g^+ . In other words, the deformation in the mean flow intensified with a greater degree of surface manipulation on the bottom wall. This is reasonable since larger V-groove riblets should impose stronger gradients on the mean flow.

The choice of power law index $p = 0.26$ in Fig. 19(b) seems to coincide with the Blasius scaling used in the empirical relation concerning the skin friction coefficient at low Reynolds number [66]: $C_f = 0.073Re_m^{-0.25}$. More recently, a theoretical analysis [67] shows that $C_f \propto Re^{-\theta}$, where $\theta = 0.26 \sim 0.27$. One possible reason why the power law index $p = 0.26$ is found to fit the available data well is probably because \mathcal{D} and C_f are both derived from the same time-averaged velocity gradient tensor. Hence, the Blasius scaling should collapse the profiles at two distinct Reynolds numbers, despite the presence of riblets in the channel. Having said that, it should be noted that the number of riblet configurations reported in this work

may not be a representative set of data. Nevertheless, the present work has explored and demonstrated the potential and appeal of using the alternative length scale l_g^+ in describing the turbulent channel flow subjected to the manipulation of V-groove riblets.

IV. CONCLUSIONS

A parametric DNS study comprises of six V-groove riblet configurations of different sizes has been carried out in a low Reynolds number turbulent channel flow setting. The simulations intend to investigate the evolution of the flow dynamics when subjected to a systematic change in the riblet size measured by l_g^+ . In all, the present set of simulations at either $Re_m = 1842$ or 2800 has confirmed that l_g^+ can also provide a better characterization of the flow field over V-groove riblets, apart from the improved scaling of drag reduction curves. Even when the ratio of h/s is not constant, the flow dynamics is found to evolve systematically with l_g^+ , which could not be achieved when using either s^+ or h^+ alone. In this respect, l_g^+ is more suitable as the effective Reynolds number that governs the local flow physics near V-groove riblets. By analyzing the six riblet configurations of various l_g^+ , it is found that the flow dynamics has a dependency on the nature of flow features arising from fluid-riblet interaction.

At the lower end of the range of l_g^+ considered, the profiles of turbulence statistics mostly resemble the baseline plane channel flow, except for a systematic shift in accordance with the groove size. Although some lodging of near-wall flow structures may happen from time to time, the fluid motions in the groove are less affected by such phenomenon. At the same time, the mean secondary flow is weaker, while its region of influence is narrower, and further away from the groove. The likelihood of flow structures to lodge in the riblet groove appears to be proportional to l_g^+ . Likewise, the strength and the degree of penetration of the induced mean secondary flow scale with l_g^+ . In particular, the secondary flow becomes increasingly prominent when $l_g^+ > 15 \sim 19$, and this coincides with the more notable enhancement of spanwise velocity fluctuations w'_{rms} .

The lodging of flow structures in the groove and the induced mean secondary flow seem to be inter-related and act hand-in-hand to cause complex and intense near-wall turbulent motions, which manifest as humps on the statistical profiles. Additionally, their increasing dominance appears to correlate with the rise in viscous drag. In those configurations with

$l_g^+ > 30$, the pronounced impact of secondary flow produces a sign inversion of the Reynolds stress in some part of the groove, while the induced downwash may in part cause the entrainment of flow structures inside the groove. Two new correlations in terms of l_g^+ are examined to illustrate the potential and appeal of l_g^+ in correlating the riblet size and the regulated flow field properties.

Since the present simulations have only considered six configurations of V-groove riblets, more extensive assessments that consider riblets of various sizes and shapes, and at a higher range of Reynolds numbers would be desirable. Such study can potentially help to pinpoint the important flow features or mechanisms that dictate the flow attributes, and to provide useful knowledge for utilizing structured surface pattern in a wide range of fluid flow applications. One interesting issue is to determine the geometrical parameters, apart from the groove size, that affect the lodging of near-wall flow structures and the generation of mean secondary flow, as well as their extent of influence on the fluid motions in the groove. More importantly, their impact on the viscous drag should be assessed via suitable means.

The authors wish to acknowledge supports from the National University of Singapore and the Ministry of Education, Singapore.

-
- [1] M. Gad-el-Hak, “Drag reduction,” in *Flow Control: Passive, Active, and Reactive Flow Management* (Cambridge University Press, New York, 2000) pp. 205–228.
 - [2] D. M. Bushnell, “Aircraft drag reduction - a review,” *Proceedings of the Institution of Mechanical Engineers, Part G: Journal of Aerospace Engineering* **217**, 1–18 (2003).
 - [3] R. Ramachandran, N. Maani, V. L. Rayz, and M. Nosonovsky, “Vibrations and spatial patterns in biomimetic surfaces: Using the shark-skin effect to control blood clotting,” *Philosophical Transactions of the Royal Society A: Mathematical, Physical and Engineering Sciences* **374** (2016).
 - [4] L. Chen, D. Han, and L. Jiang, “On improving blood compatibility: From bioinspired to synthetic design and fabrication of biointerfacial topography at micro/nano scales,” *Colloids and Surfaces B: Biointerfaces* **85**, 2–7 (2011).
 - [5] A. Pollard, “Passive and active control of near-wall turbulence,” *Progress in Aerospace Sci-*

- ences **33**, 689–708 (1998).
- [6] D. W. Bechert, M. Bruse, W. Hage, and R. Meyer, “Fluid mechanics of biological surfaces and their technological application,” *Naturwissenschaften* **87**, 157–171 (2000).
 - [7] K.-S. Choi, “Turbulent drag-reduction mechanisms: Strategies for turbulence management,” in *Turbulence Structure and Modulation*, edited by A. Soldati and R. Monti (Springer Vienna, Vienna, 2001) pp. 161–212.
 - [8] P. R. Viswanath, “Aircraft viscous drag reduction using riblets,” *Progress in Aerospace Sciences* **38**, 571–600 (2002).
 - [9] G. E. Karniadakis and K. S. Choi, “Mechanisms on transverse motions in turbulent wall flows,” *Annual Review of Fluid Mechanics* **35**, 45–62 (2003).
 - [10] B. Dean and B. Bhushan, “Shark-skin surfaces for fluid-drag reduction in turbulent flow: A review,” *Philosophical Transactions of the Royal Society A: Mathematical, Physical and Engineering Sciences* **368**, 4775–4806 (2010).
 - [11] M. J. Walsh, “Riblets as a viscous drag reduction technique,” *AIAA Journal* **21**, 485–486 (1983).
 - [12] M. Bruse, D. W. Bechert, J. G. T. van der Hoeven, W. Hage, and G. Hoppe, “Experiments with conventional and with novel adjustable drag-reducing surfaces,” in *Near-Wall Turbulent Flows*, edited by R. M. C. So, C. G. Speziale, and B. E. Launder (Elsevier, Amsterdam ; New York, 1993).
 - [13] R. García-Mayoral and J. Jiménez, “Drag reduction by riblets,” *Philosophical Transactions of the Royal Society A: Mathematical, Physical and Engineering Sciences* **369**, 1412–1427 (2011).
 - [14] M. J. Walsh and A. M. Lindemann, “Optimization and application of riblets for turbulent drag reduction,” in *22nd Aerospace Sciences Meeting* (American Institute of Aeronautics and Astronautics, Reno, Nevada, 1984) pp. 1–10.
 - [15] M. J. Walsh, “Effect of detailed surface geometry on riblet drag reduction performance,” *Journal of Aircraft* **27**, 572–573 (1990).
 - [16] D. W. Bechert, M. Bruse, W. Hage, J. G. T. Van Der Hoeven, and G. Hoppe, “Experiments on drag-reducing surfaces and their optimization with an adjustable geometry,” *Journal of Fluid Mechanics* **338**, 59–87 (1997).
 - [17] D. W. Bechert and M. Bartenwerfer, “The viscous flow on surfaces with longitudinal ribs,”

- Journal of Fluid Mechanics **206**, 105–129 (1989).
- [18] D. W. Bechert, M. Bartenwerfer, and G. Hoppe, “Turbulent drag reduction by nonplanar surfaces - A survey on the research at TU/DLR Berlin,” in *Structure of Turbulence and Drag Reduction*, edited by A. Gyr (Springer Berlin Heidelberg, 1990) pp. 525–543.
 - [19] P. Luchini, F. Manzo, and A. Pozzi, “Resistance of a grooved surface to parallel flow and cross-flow,” Journal of Fluid Mechanics **228**, 87–109 (1991).
 - [20] H. Choi, P. Moin, and J. Kim, “Direct numerical simulation of turbulent flow over riblets,” Journal of Fluid Mechanics **255**, 503–539 (1993).
 - [21] D. B. Goldstein and T. C. Tuan, “Secondary flow induced by riblets,” Journal of Fluid Mechanics **363**, 115–151 (1998).
 - [22] R. García-Mayoral and J. Jiménez, “Hydrodynamic stability and breakdown of the viscous regime over riblets,” Journal of Fluid Mechanics **678**, 317–347 (2011).
 - [23] J. H. Ng, R. K. Jaiman, and T. T. Lim, “Direct numerical simulations of riblets in a fully-developed turbulent channel flow: Effects of geometry,” in *Advances in Computation, Modeling and Control of Transitional and Turbulent Flows* (World Scientific, Singapore, 2015) pp. 155–165.
 - [24] H. Choi, P. Moin, and J. Kim, “On the effect of riblets in fully developed laminar channel flows,” Physics of Fluids A **3**, 1892–1896 (1991).
 - [25] D. C. Chu and G. E. Karniadakis, “A direct numerical simulation of laminar and turbulent flow over riblet-mounted surfaces,” Journal of Fluid Mechanics **250**, 1–42 (1993).
 - [26] P. F. Fischer, J. W. Lottes, and S. G. nek5000 Kerkemeier, “Nek5000 web page nek5000,” <http://nek5000.mcs.anl.gov> (2008).
 - [27] A. T. Patera, “A spectral element method for fluid dynamics: Laminar flow in a channel expansion,” Journal of Computational Physics **54**, 468–488 (1984).
 - [28] M. O. Deville, P. F. Fischer, and E. H. Mund, *High-Order Methods for Incompressible Fluid Flow* (Cambridge University Press, Cambridge, United Kingdom, 2002).
 - [29] P. F. Fischer and A. T. Patera, “Parallel spectral element methods for the incompressible Navier-Stokes equations,” in *Solution of Superlarge Problems in Computational Mechanics*, edited by J. H. Kane, A. D. Carlson, and D. L. Cox (Plenum Press, New York, 1989) pp. 49–65.
 - [30] Y. Maday and A. T. Patera, “Spectral element methods for the incompressible Navier-Stokes

- equations,” in *State-of-the-Art Surveys on Computational Mechanics* (American Society of Mechanical Engineers, New York, United States, 1989) pp. 71–143.
- [31] Y. Maday, A. T. Patera, and E. M. Rønquist, “An Operator-integration-factor splitting method for time-dependent problems: Application to incompressible fluid flow,” *Journal of Scientific Computing* **5**, 263–292 (1990).
 - [32] P. F. Fischer, G. W. Kruse, and F. Loth, “Spectral element methods for transitional flows in complex geometries,” *Journal of Scientific Computing* **17**, 81–98 (2002).
 - [33] P. F. Fischer and E. M. Rønquist, “Spectral element methods for large scale parallel Navier-Stokes calculations,” *Computer Methods in Applied Mechanics and Engineering* **116**, 69–76 (1994).
 - [34] P. F. Fischer, “An overlapping Schwarz method for spectral element solution of the incompressible Navier-Stokes equations,” *Journal of Computational Physics* **133**, 84–101 (1997).
 - [35] P. Moin and K. Mahesh, “Direct numerical simulation: A tool in turbulence research,” *Annual Review of Fluid Mechanics* **30**, 539–578 (1998).
 - [36] R. García-Mayoral and J. Jiménez, “Scaling of turbulent structures in riblet channels up to $Re_\tau \approx 550$,” *Physics of Fluids* **24**, 105101–10 (2012).
 - [37] I. Marusic, B. J. McKeon, P. A. Monkewitz, H. M. Nagib, A. J. Smits, and K. R. Sreenivasan, “Wall-bounded turbulent flows at high Reynolds numbers: Recent advances and key issues,” *Physics of Fluids* **22**, 065103–24 (2010).
 - [38] A. J. Smits, B. J. McKeon, and I. Marusic, “High-Reynolds number wall turbulence,” *Annual Review of Fluid Mechanics* **43**, 353–375 (2011).
 - [39] J. Jiménez and P. Moin, “Minimal flow unit in near-wall turbulence,” *Journal of Fluid Mechanics* **225**, 213–240 (1991).
 - [40] D. Gatti and M. Quadrio, “Performance losses of drag-reducing spanwise forcing at moderate values of the Reynolds number,” *Physics of Fluids* **25**, 125109–17 (2013).
 - [41] G. E. Karniadakis and S. J. Sherwin, *Spectral/hp element methods for computational fluid dynamics*, 2nd ed. (Oxford University Press, Oxford, 2005).
 - [42] O. Pironneau, “On the transport-diffusion algorithm and its applications to the Navier-Stokes equations,” *Numerische Mathematik* **38**, 309–332 (1982).
 - [43] O. Flores and J. Jiménez, “Hierarchy of minimal flow units in the logarithmic layer,” *Physics of Fluids* **22**, 0717041–4 (2010).

- [44] A. Lozano-Durán and J. Jiménez, “Effect of the computational domain on direct simulations of turbulent channels up to $Re_\tau = 4200$,” *Physics of Fluids* **26**, 011702–7 (2014).
- [45] N. N. Mansour, J. Kim, and P. Moin, “Reynolds-stress and dissipation-rate budgets in a turbulent channel flow,” *Journal of Fluid Mechanics* **194**, 15–44 (1988).
- [46] J. Jiménez and R. D. Moser, “What are we learning from simulating wall turbulence?” *Philosophical Transactions of the Royal Society A: Mathematical, Physical and Engineering Sciences* **365**, 715–732 (2007).
- [47] J. L. Lumley and A. M. Yaglom, “A century of turbulence,” *Flow, Turbulence and Combustion* **66**, 241–286 (2001).
- [48] J. Kim, P. Moin, and R. Moser, “Turbulence statistics in fully developed channel flow at low Reynolds number,” *Journal of Fluid Mechanics* **177**, 133–166 (1987).
- [49] K. Iwamoto, Y. Suzuki, and N. Kasagi, “Reynolds number effect on wall turbulence: Toward effective feedback control,” *International Journal of Heat and Fluid Flow* **23**, 678–689 (2002).
- [50] R. García-Mayoral, *The Interaction of Riblets with Wall-Bounded Turbulence*, Ph.D. thesis, Universidad Politécnica de Madrid (2011).
- [51] R. Grüneberger and W. Hage, “Drag characteristics of longitudinal and transverse riblets at low dimensionless spacings,” *Experiments in Fluids* **50**, 363–373 (2011).
- [52] D. McLean, *Understanding Aerodynamics: Arguing from the Real Physics* (Wiley, United Kingdom, 2013).
- [53] M. J. Walsh, “Riblets,” in *Progress in Astronautics and Aeronautics: Viscous Drag Reduction in Boundary Layers*, Vol. 123, edited by D. M. Bushnell and J. N. Hefner (American Institute of Aeronautics and Astronautics, Washington, DC, 1990) pp. 203–261.
- [54] P. R. Spalart, “Direct simulation of a turbulent boundary layer up to $Re_\theta = 1410$,” *Journal of Fluid Mechanics* **187**, 61–98 (1988).
- [55] R. D. Moser, J. Kim, and N. N. Mansour, “Direct numerical simulation of turbulent channel flow up to $Re_\tau = 590$,” *Physics of Fluids* **11**, 943–945 (1999).
- [56] S. Tardu, T. V. Truong, and B. Tanguay, “Bursting and structure of the turbulence in an internal flow manipulated by riblets,” *Applied Scientific Research* **50**, 189–213 (1993).
- [57] K. Fukagata, K. Iwamoto, and N. Kasagi, “Contribution of Reynolds stress distribution to the skin friction in wall-bounded flows,” *Physics of Fluids* **14**, L73–L76 (2002).
- [58] I. Marusic, D. D. Joseph, and K. Mahesh, “Laminar and turbulent comparisons for channel

- flow and flow control,” *Journal of Fluid Mechanics* **570**, 467–477 (2007).
- [59] D. Goldstein, R. Handler, and L. Sirovich, “Direct numerical simulation of turbulent flow over a modelled riblet covered surface,” *Journal of Fluid Mechanics* **302**, 333–376 (1995).
 - [60] J. M. Wallace, “Quadrant analysis in turbulence research: History and evolution,” *Annual Review of Fluid Mechanics* **48**, 131–158 (2016).
 - [61] S. J. Lee and S. H. Lee, “Flow field analysis of a turbulent boundary layer over a riblet surface,” *Experiments in Fluids* **30**, 153–166 (2001).
 - [62] O. A. El-Samni, H. H. Chun, and H. S. Yoon, “Drag reduction of turbulent flow over thin rectangular riblets,” *International Journal of Engineering Science* **45**, 436–454 (2007).
 - [63] A. E. Perry, M. S. Chong, and T. T. Lim, “The vortex-shedding process behind two-dimensional bluff bodies,” *Journal of Fluid Mechanics* **116**, 77–90 (1982).
 - [64] C. H. Crawford and G. E. Karniadakis, “Reynolds stress analysis of controlled wall-bounded turbulence,” in *27th AIAA Fluid Dynamics Conference* (American Institute of Aeronautics and Astronautics, New Orleans, LA, 1996) pp. 1–12.
 - [65] K. Iwamoto, K. Fukagata, N. Kasagi, and Y. Suzuki, “Friction drag reduction achievable by near-wall turbulence manipulation at high Reynolds numbers,” *Physics of Fluids* **17**, 011702–4 (2005).
 - [66] R. B. Dean, “Reynolds number dependence of skin friction and other bulk flow variables in two-dimensional rectangular duct flow,” *Journal of Fluids Engineering* **100**, 215–223 (1978).
 - [67] V. Yakhot, S. C. C. Bailey, and A. J. Smits, “Scaling of global properties of turbulence and skin friction in pipe and channel flows,” *Journal of Fluid Mechanics* **652**, 65–73 (2010).